

July 2011

Interstellar Silicate Dust in the $z=0.89$ Absorber Towards PKS 1830-211: Crystalline Silicates at High Redshift?

Monique C. Aller

*Department of Physics & Astronomy, University of South Carolina, 712 Main Street, Columbia, SC 29208,
USA*

ALLERM@mailbox.sc.edu

Varsha P. Kulkarni

*Department of Physics & Astronomy, University of South Carolina, 712 Main Street, Columbia, SC 29208,
USA*

Donald G. York

*Department of Astronomy & Astrophysics, University of Chicago, 5640 S. Elis Ave., Chicago, IL 60637,
USA*

Giovanni Vladilo

Osservatorio Astronomico di Trieste, Via Tiepolo 11 34143 Trieste, Italy

Daniel E. Welty

*Department of Astronomy, University of Illinois, Urbana-Champaign, 215 Astronomy Building, MC-221,
1002 W. Green St. Urbana, IL 61801, USA*

and

Debopam Som

*Department of Physics & Astronomy, University of South Carolina, 712 Main Street, Columbia, SC 29208,
USA*

ABSTRACT

We present evidence of a $>10\text{-}\sigma$ detection of the $10\text{ }\mu\text{m}$ silicate dust absorption feature in the spectrum of the gravitationally lensed quasar PKS 1830-211, produced by a foreground absorption system at redshift 0.886. We have examined close to 100 optical depth templates, derived from both observations of Galactic and extragalactic sources and laboratory measurements, in order to constrain the chemical structure of the silicate dust. We find that the best fit to the observed absorption profile is produced by laboratory crystalline olivine, with a corresponding peak optical depth of $\tau_{10} = 0.24 \pm 0.05$. The fit is slightly improved upon by including small contributions from additional materials such as silica and serpentine, which suggests that the dust composition may consist of a blend of crystalline silicates. Combining amorphous and crystalline templates, we find that the fraction of crystalline silicates needs to be at least 95%. Given the rarity of extragalactic sources with such a high degree of silicate crystallinity, we also explore the possibility that

the observed spectral features are produced by amorphous silicates in combination with other molecular or atomic transitions, or by foreground source contamination. While we cannot rule out these latter possibilities, the profile fits are much poorer than for the crystalline olivine template. If the presence of crystalline interstellar silicates in this distant galaxy is real, it would be highly unusual, given that the Milky Way interstellar matter contains essentially only amorphous silicates. It is possible that the $z=0.886$ absorber towards PKS 1830-211, well known for its high molecular content, has a unique star-forming environment that enables crystalline silicates to form and prevail.

Subject headings: dust: extinction - galaxies: ISM - quasars: absorption

1. INTRODUCTION

Dust is a significant constituent of the observable universe, both impacting the appearance of galaxies and influencing their evolution. It affects the derived properties of some galaxies by attenuating the shorter-wavelength radiation emitted by stars and ionized gases, and re-emitting this radiation at longer wavelengths; more than 30% of the energy emitted as starlight is re-radiated in the IR by dust (Bernstein et al. 2002). Furthermore, dust influences physical processes in the interstellar medium (ISM) ranging from heating, cooling, and ionization processes, to those dictating the production of molecules and the formation of stars. Thus, understanding the nature of extragalactic interstellar dust grains is essential for characterizing the chemical evolution of galaxies, and for correcting the observations of local and high redshift objects used in studies spanning topics from galaxy morphology to cosmology.

Despite the fundamental importance of dust in analyses characterizing galaxy evolution, however, there remain many open questions about the distribution and composition of dust in non-local galaxies, and about the possible cosmological evolution of dust properties. While significant evidence of dust-enshrouded star-formation has been found in far-IR and sub-mm studies of galaxies at moderate redshifts (Barger et al. 1998; Elbaz et al. 1998; Chary & Elbaz 2001), detailed extinction curves have only been measured for a small number of local group galaxies, such as the Milky Way (MW), SMC, and LMC, and for a subset of local starburst galaxies (Pei 1992; Calzetti et al. 2000). The local ISM can be studied both directly, through extinction and IR emission/absorption, and indirectly, via depletions inferred from gas-phase abundances. These studies reveal environmental variations in even local dust grain properties, such as differences in the dust-to-gas ratios, UV extinctions, and depletion patterns observed in the lower metallicity Magellanic Clouds (Welty et al. 2001; Gordon et al. 2003; Sofia et al. 2006), that are not fully understood. At higher redshift our understanding is even more incomplete, with limited direct knowledge about the detailed properties of dust in regular galaxies. The simplistic assumption that high-redshift dust grains are similar in size and composition to local dust may impact both derived galaxy properties, particularly in on-going large-scale galaxy surveys (e.g. SDSS, COSMOS), and techniques which are sensitive to the effects of dust attenuation, such as the Type Ia supernova studies used to infer the acceleration of the cosmic expansion [e.g., Aguirre (1999a,b); Riess et al. (2004)].

One technique which may be exploited to provide insight into the chemical composition of high-redshift ISM dust is the examination of absorption line systems in quasar spectra; particularly those in damped Lyman-alpha (DLA) absorption systems. These neutral-hydrogen rich systems ($\log N_{HI} > 20.3$) contain a substantial fraction of the neutral gas in galaxies (Wolfe et al. 1995; Storrie-Lombardi & Wolfe 2000), and are considered to be the best indicators of the chemical content of high redshift galaxies (Pettini et al. 1994;

Prochaska et al. 2003; Kulkarni et al. 2005). Furthermore, since DLAs are selected solely by gas cross-section, rather than by galaxy brightness, they provide a relatively unbiased direct probe of dust in high redshift systems (Ostriker et al. 1990; Fall et al. 1993). Evidence for the presence of dust in DLA systems comes from both measured depletions of refractory elements, and from the detected reddening of background quasars (Pei et al. 1991; Pettini et al. 1997); a study of >800 SDSS quasar spectra has found clear evidence of an association of quasar reddening with absorption line strengths at $1 < z < 2$ (York et al. 2006). Dust in DLAs is also indirectly suggested by recent analyses (Kulkarni et al. 2005, 2007a, 2011; Péroux et al. 2006, 2011; Prochaska et al. 2006) which find that the majority of DLAs exhibit low metallicities and low star-formation rates (SFRs). This finding is in contradiction to chemical evolution model predictions (Pei et al. 1999; Somerville et al. 2001) that are based on the cosmic star-formation history as inferred from galaxy imaging surveys (e.g. the Hubble Deep Field, Madau et al. (1996)). A scenario (Fall et al. 1993; Boissé et al. 1998; Vladilo & Péroux 2005) in which the more dusty and more metal-rich DLAs provide greater obscuration of their background quasars, hence impeding their detection, could explain these findings.

One of the primary open questions about high-redshift dust, which may be probed using DLA systems, pertains to the chemical composition and size distribution of the dust grains. Models for local dust generally assume a mixture of carbonaceous, silicate, and metallic/oxide grains with a given distribution of grain sizes. In the Milky Way, more than 70% of the core mass of interstellar dust is found in silicate grains. These silicate grains are produced only when oxygen is more abundant than carbon; the excess of silicate dust measured in the MW galactic center has generally been attributed to a shortage of carbon-rich stars. At high redshift, however, most studies have focused only on characterizing carbonaceous dust, by probing either the 2175Å feature or the shape of the rest-frame UV extinction curve. Recent studies, by our group, examining quasar absorbers using the Spitzer InfraRed Spectrograph (IRS) though, have found clear detections of the 10 μm silicate dust feature in these objects, with an $\gtrsim 10\text{-}\sigma$ detection in the AO 0235+164 DLA system (Kulkarni et al. 2007b, 2011). These analyses suggest that the overall shape of the silicate absorption feature is best fit by an optical depth profile template derived from either laboratory amorphous olivine or from diffuse Galactic interstellar clouds, rather than from dense molecular clouds. These studies also find that the silicate feature is about 2-3 times as deep as expected from an extrapolation of the $\tau_{10}\text{-}A_V$ relationship for MW diffuse ISM clouds, suggesting that these systems may be probing dust in the inner regions of their respective absorbing host galaxies, rather than dust on the outskirts.

In light of this recent success in detecting silicate dust in DLAs towards distant, moderately reddened quasars, we have now selected the 10 μm silicate feature in the PKS 1830-211 quasar absorption system for study. This particular DLA has been targeted for several reasons. First, the illuminating $z=2.507$ quasar is strongly lensed by a foreground ($z=0.886$), late-type (Sbc), low-inclination spiral, which is the presumed DLA host galaxy (Winn et al. 2002; Courbin et al. 2002; Wilkind & Combes 1998). This lensing produces two distinct images of the quasar; a brighter (NE) component with a magnification of 5.9, and a second (SW) component which provides 1.5 times less magnification and exhibits signatures of dustier, more molecule-rich material (Winn et al. 2002). Towards the NE component and in the absorber disk $N_{HI} \sim 2\text{-}3 \times 10^{21} \text{ cm}^{-2}$, assuming $T_{spin}=100\text{K}$ (Chengalur 1999; Koopmans & de Bruyn 2005), with a density of $N(H_2) = 1700 - 2600 \text{ cm}^{-3}$ towards the more obscured SW component (Henkel et al. 2009). While the spatial resolution of the Spitzer IRS is unable to separate these two lines of sight through the host galaxy, their integrated combination provides a significantly stronger quasar continuum detection, and resultant signal-to-noise ratio (SNR) for the silicate feature, than has been obtained for the previous analyses of silicate dust in DLAs (Kulkarni et al. 2007b, 2011). Second, while the majority of DLAs have relatively low amounts of dust, this source is part of a small subset of DLAs found through radio/mm surveys to be a molecularly-rich, 21-cm (HI) absorber (Chengalur 1999), indicative of an especially dusty and chemically more evolved DLA

system. Further evidence for the high dust content is provided by the relatively high measured absorber-frame extinction ($A_V < 4.1$) and by the ratio of the total to selective extinction ($R_V = 6.34 \pm 0.16$) for this system (Falco et al. 1999). The high absorber rest-frame reddening of $E(B-V) = 0.57 \pm 0.13$, with $\Delta E(B-V) = 3.00 \pm 0.13$ between the two quasar sight lines, is more typical of values found for sub-mm selected SCUBA sources (~ 0.55) than for either Lyman-break galaxies [0-0.45 with a median of 0.16 at $z \sim 3$; Shapley et al. (2001); Papovich et al. (2001)] or MgII absorbers [0.002; York et al. (2006)]. Thus, dusty absorbers such as this system may provide part of an evolutionary link in the sequence of SFRs, masses, metallicities, and dust content connecting the generally metal- and dust-poor general DLA population (detected in absorption) with low SFRs to the actively star-forming metal- and dust-rich Lyman-break galaxies (detected in emission). Third, the PKS 1830-211 system is known to exhibit sub-mm absorption features revealing the presence of a multitude of molecules, in many cases in multiple transitions, including HCN, HCO⁺, ortho-H₂CO, HNC, NH₃, N₂H⁺, H¹³CO⁺, H¹³CN, CO, CS, C I, ¹³CO, and C¹⁸O [e.g. Wilkind & Combes (1996, 1998); Bottinelli et al. (2009); Henkel et al. (2008); Menten et al. (2008); Muller & Guélin (2008)]. This abundance of molecules is suggestive of a chemically rich environment for the DLA system, which we anticipate may be characteristic of systems which contribute significantly to the global metal content.

We begin our paper with a description of our observations and data reductions in §2, and then in §3 present our analysis utilizing the laboratory and observationally-derived silicate profile templates to estimate the optical depth in the 10 μm silicate absorption feature towards PKS 1830-211. We discuss in §4 the implications of our finding that the prominently detected 10 μm silicate dust feature present in the PKS 1830-211 absorber has a crystalline silicate composition. Finally, we summarize our results in §5. In Appendix A we address two minor observational caveats which could potentially affect our analysis.

2. DATA & ANALYSIS

2.1. Observations and Reductions

Our observations, summarized in Table 1, were obtained using the InfraRed Spectrograph (IRS) on the Spitzer Space Telescope (Werner et al. 2004). These data consist of 69 individual spectral exposures, each observed in two nod positions, totaling 198 minutes (3.3 hours) of integration on-target, centered at $(\alpha, \delta) = (18\text{h}33\text{m}39.89\text{s}, -21\text{d}03\text{m}40.4\text{s})$. The two nods, obtained using the IRS Staring mode, facilitate both background subtraction and the identification of spectral features induced by bad pixels. Given the spectral breadth of the silicate spectral features in previous DLAs (Kulkarni et al. 2007b, 2011), we chose to utilize the low-resolution mode ($R \sim 60-130$), rather than the high-resolution mode ($R \sim 600$), in order to reach a higher sensitivity (Houck et al. 2004). In addition to the LL1/2 and SL1/2 spectra, bonus (third) order SL and LL spectra were obtained, which facilitate normalization of the first and second order spectra, as described below. Our complete data set spans a spectral region from 5.13 to 39.90 μm ; this broad wavelength coverage is crucial for the accurate determination of the continuum which we require to measure the strength of the broad silicate features.

The IRS slit cannot individually distinguish the two lensed PKS 1830-211 quasar images. The lower-wavelength data (SL) are obtained with an $3.''6-3.''7 \times 57''$ slit and a $1.''8/\text{pixel}$ scale Si:As CCD, while the longer-wavelength data (LL) are obtained with a $10.''65-10.''7 \times 168''$ slit and a $5.''1/\text{pixel}$ scale Si:Sb CCD (Houck et al. 2004). Given this resolution, we are unable to spatially differentiate the two lensed images, which are separated by $(\Delta\alpha, \Delta\delta) = (-0.''642, -0.''728)$ and embedded in a fainter Einstein ring (Winn et al. 2002). Thus, we cannot probe the two distinct lines of sight through the DLA, and instead can only address

a composite spectrum which constrains the *average* dust properties within the DLA. The NE lensed quasar image is significantly brighter at all wavelengths (Lehár 2000; Courbin et al. 2002; Winn et al. 2002), and we assume that our continuum is dominated by this line of sight. The weaker (SW) component is more heavily dust-obscured, since it passes through a region of enhanced star formation in the western spiral arm of the host (Winn et al. 2002), and will contribute more significantly to our measured silicate dust absorption, as it does in detections of molecular absorption [see e.g. Lehár (2000); Frye et al. (1997)]. Furthermore, we note that several neighboring objects are spatially inseparable from our quasar spectrum. These sources include [see illustrations in Courbin et al. (2002) and Winn et al. (2002)] an M4 dwarf star, a foreground galaxy at $z \sim 0.19$, and possibly a second star and a second galaxy close to the DLA host. As explained in Appendix §A.2, none of these other sources are expected to contribute significantly to our observed spectrum.

Our analysis utilizes the Basic Calibrated Data (BCD) reduced spectra, and associated uncertainties and bad pixel masks, produced by version 18.7.0 of the Spitzer automatic pipeline. These spectra have been bias and dark subtracted, and a characteristic flat field has been applied. Additionally, the data have been corrected for systematic effects such as droop and dark-current drift, and cosmic ray hits have been identified and flagged in the corresponding masks.

We have further processed the Spitzer BCD spectra by utilizing *IRSCLEAN* (*v1.9-2.0*) to identify and remove rogue pixels and cosmic rays, and to reduce the background noise in the frames. In addition to replacing bad/rogue pixels identified by the masks and iterative algorithms, we have implemented a slightly non-traditional application of the *IRSCLEAN* software in which we also manually identified for replacement all pixels in the spectra backgrounds with visibly high/low signal in order to smooth the background. We did not apply *IRSCLEAN*-replacements, even for noted bad pixels, within the quasar spectrum or its environs, in order to prevent any spurious spectral signatures from being added to our data by the algorithm. We then manually removed bad/rogue pixels along or near the spectrum using the *epix* task in IRAF, and replacing points with the median of the surrounding pixels. For pixels along the quasar spectrum, the unweighted average of bordering points along the spectral axis were used instead of the median. We were generally conservative with identifying and replacing these pixels, and only targeted strongly discrepant points, e.g. those pixels with saturated flux or isolated pixels with substantially higher/lower values than neighboring pixels. Pixels producing all other visible spectral features were retained as plausibly physical in origin, and those which were not intrinsic to the data were effectively removed when we combined the data from the two nod positions. Additionally, we applied the IRAF task *fixpix* to smooth over two weak foreground stellar spectra present in the off-target LL1 spectra; these frames were utilized for background subtraction as described below.

We combined the cleaned individual BCD exposures in each nod position using the IDL script *coad*, which automatically propagates the uncertainties and mask files, and then subtracted the backgrounds using the IRAF task *imarith*, propagating the uncertainties in quadrature. For the SL data we subtracted one nod position from the other, in order to remove the background contribution. For the LL data, however, there exists an anomalous scattered light feature (see Appendix A.1). This spatially-broad and intense feature prevented us from subtracting the two nods to remove the background. Therefore, we combined with *coad* all of the off-target LL1 frames (obtained while the quasar was in the LL2 order) and vice-versa to create off-target background frames, which were then subtracted from the spectra in each nod position.

2.2. Spectral Extraction and Normalization

We extracted the one-dimensional spectra for each order using the Spitzer IRS Custom Extractor (*SPICE*) algorithm, set for a point source extraction with optimal-weighting, using the default extraction aperture in each order, with no subsequent corrections for fringing. Our final extracted spectra have a varying spatial width over the dispersion axis, as per the standard *SPICE* templates, sampling a broader spatial extent at the longest wavelengths within each order. The visual inspection of the two-dimensional spectra prior to extraction showed no apparent fringing in the SL or LL2 spectra, and only weak fringing in LL1. The *IRSFRINGE* manual stipulates that fringes are not spectrally resolved in the SL module, while in the LL module fringes resulting from one of the filters are present in the raw un-calibrated data, with an amplitude of 3-10%, depending on wavelength. These are generally largely corrected through the applied pipeline flat-fielding. As a test, we applied the *IRSFRINGE* (*v. 1.1*) algorithm to our extracted LL data and found that the algorithm did not automatically detect any significant fringes, and when forced to correct for any measurable fringes, produced only a negligible statistical and visual improvement in the data quality, with small spurious spectral features resulting in a few cases. Therefore, we have applied no fringe corrections to our extracted spectra.

In order to improve the SNR for our spectra, we have combined the one-dimensional extracted spectra from each of the two spectral nod positions in an unweighted average. The uncertainties have been propagated in quadrature, and reflect both the measurement uncertainty produced through the BCD pipeline reductions, and the scatter of the two nods relative to their mean. These uncertainties are dominated by variations between the two nod positions. While the spectra extracted from the two nod positions are generally consistent, there exist regions with small discrepancies where e.g. one of the nods exhibits a convex feature, while the other exhibits a concave feature. These small variations are at most 10% relative to the mean spectrum in the SL and LL2 data. In the LL1 data, a discrepancy on the order of $\pm 15\text{-}20\%$ is observed over an extended spectral region from $\sim 22\text{-}26 \mu\text{m}$; this feature does not affect our measurements of the 10 and 18 μm features in the $z=0.886$ absorber. After consultation with the Spitzer Science Center staff, we conclude that the origin of this feature is likely scattered light, as discussed in the Appendix A.1.

We have manually trimmed the nod-combined spectra in order to eliminate visually discrepant and noisy points. The majority of these removed points represent isolated data points where a bad pixel in one of the nods was not removed through our conservative spectral cleaning (§2.1), occur in regions where the two nods showed discrepant spectral features, or occur beyond 38 μm where the noise notably increases. We have also eliminated points at the edges of each spectral order which do not connect smoothly with the adjoining orders. The exclusion of these data points does not significantly impact our derived fits and conclusions.

Finally, we have normalized and joined the data in the four SL-LL spectral orders to form a single spectrum for the PKS 1830-211 system, which is illustrated in Figure 1. Within the SL and LL orders we have normalized the first and second order data to the bonus (third) order. The individual data points from the bonus orders have been excluded from our final spectrum, as they align with the data in the retained spectral orders and exhibit similar features within the overlapping spectral regions. We also note that the joining of the LL1 and LL2 spectral orders occurs within the 10 μm feature of our $z=0.886$ absorber, which is the focus of our analysis, and so could potentially impact the shape of this feature; however, as the orders align well and match the bonus order spectrum, we do not believe that the observed structure illustrated in Figure 1 is a result of this joining. We have then joined the LL data to the SL data by scaling down the LL data to match. An examination of longer (radio) and shorter (X-ray) wavelength data from the literature does not convincingly argue for either scaling up the SL data or scaling down the LL data. Since the SL

data generally have smaller associated formal uncertainties, we have given that order preference in setting the absolute-flux-normalization. This has resulted in final normalization-scaling factors of 0.97, 0.99, 0.91, and 0.87 relative to the original extracted data for the SL2, SL1, LL2, and LL1 data respectively. These scaling factors are consistent with scalings employed in other analyses [e.g., Spoon et al. (2006)]. Since our analysis is based on a quasar-continuum-normalized spectrum, any offsets in the absolute flux normalization will not impact our conclusions. Lastly, our normalized data have been shifted to the rest frame of the DLA host, assuming an absorber wavelength of 0.886, and all figures depict the absorber-rest-frame wavelength.

In order to ascertain which of the silicate template profiles (§3.1) best represent the silicate absorption features, we have normalized our spectrum by a fit to the quasar continuum. We have examined PKS1830-211 data at both longer (radio) and shorter (X-ray) wavelengths to ascertain whether a single quasar continuum could be fit through an extended frequency range, but given the discrepancies and variability in the literature data, particularly at radio wavelengths, and the large wavelength separation between our data and this supplementary data, we decided to select a continuum which fits in detail solely our own IR data. While Kulkarni et al. (2007b, 2011) found that either a polynomial or a power-law fit was able to represent the quasar continuum in analyses of other quasar absorption systems, in the case of PKS 1830-211 neither a power-law nor a linear fit adequately represents our continuum. As an alternative, we explored Chebyshev 3rd-5th order polynomial, Legendre 3rd order polynomial, and single-component cubic spline fits to the continuum, and determined that the best fit was obtained using a third order Chebyshev polynomial. These fits were obtained using the IRAF task *continuum* with unweighted fitting in linear-space and no averaging of the sample points. We experimented with both manually masking additional points within the four prominent absorption features (5.5-6.2 μm , 6.5-7.1 μm , 8.5-12.2 μm , and 14.8-18.3 μm in the absorber rest-frame), and with forcing the continuum to pass through certain points, particularly at the long wavelength end of the spectrum. In total, we considered 14 different normalizations of the quasar continuum. We determined that the 3rd order Chebyshev polynomial (see Figure 1), using maximal masking of points in the absorption regions, and forcing of the shape of the curve at the longest wavelengths, produced the best fit. This quality assessment was based on both a visual inspection of the fits and normalizations, and an examination of the reduced-chi-squared values for the amorphous olivine and crystalline olivine template fits, using each of the 14 normalizations.

Our final normalized spectrum, depicted in Figure 1, has apparent emission bumps before and after the 10 μm silicate feature, but these may be emission features in the spectrum and none of our quasar continuum fits fully removed them. The leftmost bump could potentially be produced by either PAH emission at 7.7 μm in the rest frame of the $z=0.886$ absorber, as is seen in some UltraLuminous Infrared Galaxies (ULIRGs) (Hao et al. 2007), or by an atomic transmission line, such as 4.53 μm [Ar VI] emission in the rest frame of the quasar. The rightmost bump is less pronounced and could include emission from a 6.985 μm [Ar II] line [seen weakly in some Seyferts and possibly some ULIRGs (Hao et al. 2007)], a 7.7 μm PAH emission feature, and/or other atomic/molecular transitions in the rest frame of the quasar. The lower-wavelength absorption features at 6.0 μm and 6.9 μm are likely produced by water ice (Kwok 2007) and possibly hydrocarbon molecular transitions (Spoon et al. 2006) in the absorber, respectively; although we note for this latter feature that there is no evidence for the expected companion 7.25 μm hydrocarbon band. These two features at 6.0 and 6.9 μm are visually similar to those in the spectrum of the W33A embedded protostar (Gibb et al. 2000), which were ascribed to the 6.0 μm water ice feature and to an unidentified transition. Higher resolution spectra would be useful in determining the exact line structure in all of these features, in particular for determining whether we are seeing broad emission line features, or emission features which are a blending of multiple narrower emission lines.

3. RESULTS

The PKS 1830-211 absorber produces prominent silicate absorption features at both 10 and 18 μm , as is clearly illustrated in Figure 1. We have measured the equivalent width of the 10 μm feature directly from this rest-frame, continuum-normalized spectrum. The total uncertainty associated with the calculated equivalent width includes the uncertainty from photon noise combined in quadrature with the uncertainty resulting from fitting the continuum. We have adopted a nudge factor of 0.3 (Sembach & Savage 1992), in estimating the continuum-fitting uncertainty. We find that the equivalent width of the 10 μm feature is $W_{rest} = 0.366 \pm 0.029 \mu\text{m}$, resulting in a significance of 12.7σ . If we exclude the contribution to the uncertainty from the continuum fitting, this significance would rise to a 28.4σ detection. We have not estimated the equivalent width associated with the 18 μm absorption feature, since it lies at the edge of our spectral range and may not be fully covered by the current data set.

3.1. Template Profile Fitting Procedures

In order to understand the physical origin of the 10 μm silicate feature, and the chemical composition of the dusty material, we have fitted a series of silicate template optical depth profiles (see Tables 2 and 3) to our observed spectrum. Our fitting assumes simple radiative transfer through the cloud, such that $I/I_0 = \exp[-\tau]$ where $\tau = -a_n\tau_{norm}$ and τ_{norm} is the optical depth profile for the template, normalized to have a peak depth of 1.0. The peak optical depth (i.e. a_n) for each template profile is selected to produce the minimum χ_r^2 . In order to obtain the associated 1σ error bars, we have (cubic-spline) interpolated the two values in the χ_r^2 vs. τ curve for which $\chi_r^2 - \chi_{r,min}^2 = 1$. The primary fitting has been performed over the spectral region 8.0-13.3 μm , unless the literature-based optical depth profile restricts the fitting to a narrower range (see Table 4). For those objects in which the template profile additionally covers the 18 μm silicate feature, we have performed a second fit extending though 19.45 μm , which is the maximum absorber-rest-frame wavelength retained in our PKS1830-211 spectrum following the clipping described in §2.1.

To constrain the composition of the material producing the 10 μm silicate absorption in the $z=0.886$ absorber, we fit 80 unique optical depth profiles, all extracted from the literature. These templates probe environments ranging from the solar system (comets) to circumstellar material to the diffuse interstellar medium (ISM) to dense molecular clouds to extragalactic objects (e.g. ULIRGs) to laboratory silicate profiles. These profiles have been extracted from Bernard-Salas et al. (2009); Bowey & Adamson (2001, 2002); Bowey et al. (2003); Campins & Ryan (1989); Chiar & Tielens (2006); Chiar et al. (2011); Knez et al. (2005); Roche & Aitken (1984); Speck et al. (1997); Spoon et al. (2006); and van Breemen (2011). With the exception of the laboratory measurements, all profiles are based on published observations of astrophysical objects, some of which had substantial noise, which we have smoothed prior to fitting; we have visually verified that this smoothing did not remove any significant intrinsic structural features in the profiles. These templates include a mixture of silicate feature profiles which were detected in absorption (e.g. ULIRGs and the Galactic ISM) and in emission (e.g. young stellar objects; YSOs), and we do not distinguish between these profiles in our analysis, although they reflect variations in temperature in the medium of origin. In addition to these basic 80 extracted profiles, we have generated versions of the 12 ULIRG template profiles which exclude the PAH emission features between 11-12 μm , which are not seen in our spectrum; this brings the total number of template profiles we examined to 92.

We have considered this large range of template profiles to encompass the broadest range of both the

physical environments in which silicates are detected, and of the observed silicate chemical compositions. As addressed in Bowey & Adamson (2002), the broad 10 μm feature is generally attributed to Si-O stretching in amorphous silicate material. Additional spectral features in this region are associated with either crystalline silicates or with atomic/molecular transitions (Spoon et al. 2006). The degree of crystallinity in these silicates varies widely amongst different astrophysical sources, as discussed in detail in §4, ranging from nearly 90% for some comets to nearly 0% for the ISM. Thus, our broad range of template profiles implicitly allows us to probe a range of crystalline:amorphous silicate ratios, although we do not expect that the formation mechanisms producing the silicate absorption towards PKS 1830-211 are necessarily similar to those in a circumstellar disk or comet. Reflecting the range of chemical compositions producing the putative 10 μm silicate feature, the observed profiles span a range of values for the peak feature wavelength from 9.37 μm for a YSO embedded in the Taurus molecular cloud to 10.39 μm for a star behind a dense molecular cloud. The laboratory silicate optical depth profiles show an even broader range of peaks. We note that in our PKS 1830-211 spectrum, as discussed in the following sections, the peak wavelength of the absorption feature is longward of 9.7 μm . Laboratory experiments have found that variations in grain morphology, including size, shape, porosity, agglomeration, SiO_4 polymerization, and metallicity, can substantially alter both the shape of the optical depth profile, and its peak wavelength [e.g., Henning et al. (2005); Henning (2010)].

We have selected for inclusion in this paper a representative subset of 26 of the combined 92 profiles, which are detailed in Tables 2 and 3. We illustrate these profiles in Figures 2 and 3, which visually elucidate the range in profile shapes. In each template category, we have selected for illustration those profiles which exhibit the lowest χ_r^2 fits, those which are most representative of the distributions of features characterizing the category of silicate profiles, and in a few cases, those which exhibit a unique distinguishing feature differentiating them from other profiles in the category. About half of the template profiles cover both the 10 and 18 μm silicate features; while the rest cover only the 10 μm feature.

The fits with these 26 templates are presented in Table 4 and illustrated in Figures 4 and 5. We list the peak optical depth for fitting both solely over the 8.0-13.3 μm spectral region and over the 8.0- λ_{max} μm region, where λ_{max} is the maximum wavelength covered by the data; these ranges are truncated if there is inadequate wavelength coverage for the template. The broader fitting region allows us to simultaneously fit the 10 μm silicate feature and the 18 μm silicate feature, which is partially covered by our PKS 1830-211 spectrum. Considering our complete subset of 26 profiles, we find $0.10 \leq \tau_{10} \leq 0.15$ for the observation-based profiles, and $0.09 \leq \tau_{10} \leq 0.26$ for the laboratory-based profiles. Most of these are visibly poor fits. Our best fit estimate of the peak optical depth is $\tau_{10} = 0.24 \pm 0.05$ for the crystalline olivine 1 template. As discussed below, this best fit was determined from both a visual inspection of the fits and based on the χ_r^2 , and is at the highest end of the optical depth range covered by our template profiles.

3.2. Fits with Laboratory Crystalline Silicate Templates

Our analysis finds that the best fits to the 10 μm silicate absorption feature towards PKS 1830-211 are produced by the pure laboratory crystalline silicate profiles. We examine a total of six crystalline silicate profiles which span chemical compositions including olivine, pyroxene, silica, serpentine, and a 21 crystalline silicate blend (see Ferraro (1982); Bowey & Adamson (2002).) Within our sample of 26 templates, only the crystalline silicate profiles exhibit the signature multiple-peaked optical depth structure that we observe in the PKS 1830-211 absorber spectrum near 10 μm . As illustrated in Figure 5 of Bowey & Adamson (2002), as the laboratory silicates become increasingly crystalline in structure, as opposed to amorphous, they develop additional structure within their optical depth profiles. Furthermore, as illustrated in Figure 4 of Bowey &

Adamson (2002), these silicate profiles can intrinsically span a wide range of shapes and structures, even within a single chemical composition. For this reason, we examine two different optical depth profiles for crystalline olivine excerpted from this figure, which we have termed here olivine 1 and olivine 2.

While our fits strongly suggest that crystalline silicates provide the best match to our structure-rich absorption profile, it is apparent from Figure 5 that none of the examined crystalline templates are a perfect match to the data. The best match, in terms of both χ_r^2 and visual appearance, is produced by olivine 1. However, although olivine 1 reproduces the $\sim 10 \mu\text{m}$ dip, the olivine 1 $\sim 11 \mu\text{m}$ dip is offset to slightly higher wavelengths. Conversely, the olivine 2 profile reproduces the $\sim 11 \mu\text{m}$ feature, but is offset to lower wavelengths relative to the data near the $\sim 10 \mu\text{m}$ dip. We, therefore, conclude that while crystalline olivine reproduces the bulk of the absorption profile, we have not precisely isolated the combinations of crystalline olivine grain properties which would simultaneously reproduce both absorption features.

3.2.1. Evidence for Multiple Crystalline Silicates in Combination

Furthermore, there is evidence that a second silicate material may be contributing to the feature. We note that both of the crystalline olivine profiles are slightly too shallow to fit the $\sim 10 \mu\text{m}$ dip, while simultaneously fitting the $\sim 11 \mu\text{m}$ dip, and neither of them reproduces the absorption feature present near $9 \mu\text{m}$. However, as illustrated in the bottom panels of Figure 6, crystalline silica or serpentine can produce this additional feature. The silica better reproduces the $\sim 9 \mu\text{m}$ feature, while the serpentine profile can produce a dip near the $\sim 9 \mu\text{m}$ feature, as well as contribute absorption in the (olivine-under-fitted) region of the $\sim 10 \mu\text{m}$ dip. From this we infer that the $10 \mu\text{m}$ silicate feature observed in the PKS 1830-211 absorber might best be reproduced by a combination of crystalline olivines, silicas, and possible serpentine materials. Since it appears that the $10 \mu\text{m}$ absorption feature may be produced by a combination of crystalline olivine and other silicate material, we have attempted to combine the best-fitting olivine 1 with secondary amorphous and crystalline profiles, assuming a mixture within the dusty DLA such that $I/I_0 = \exp[-(a_n\tau_{1,norm} + b_n\tau_{2,norm})]$. The optimal values for a_n and b_n are obtained simultaneously, with the uncertainties conservatively determined by ascertaining parameter values which produce $\chi_r^2 - \chi_{r,min}^2 = 1$ within a given parameter, while holding the other parameter fixed. We have also experimented with an alternate algorithm in which the a_n and b_n values are iteratively determined by holding one parameter fixed while fitting the other parameter; the results were consistent well within 1σ .

The bi-variate olivine 1 plus additional crystalline silicate fitting is not completely successful in reproducing the structure observed in our broad $10 \mu\text{m}$ silicate feature, but does reinforce our assertion that this feature is best represented by a combination of crystalline olivines and perhaps silica or serpentine material. These results are tabulated in Table 5 and illustrated in Figures 7 and 8. Unfortunately, we find that when we combine a silica or serpentine profile of adequate depth to fit the $\sim 9 \mu\text{m}$ feature, with the crystalline olivine profile, it produces too deep of a feature in the intermediate $\sim 9.5 \mu\text{m}$ region. Hence, the best χ_r^2 occurs at a compromise between fitting only one of these features well: the result is still too shallow of a fit for the $\sim 9 \mu\text{m}$ feature, but does not completely fail to fit the $\sim 9.5 \mu\text{m}$ region. This fit has a consequently low optical depth for the second constituent profile. While all of the considered bi-variate profiles provide a slight improvement in χ_r^2 over the pure crystalline olivine 1 profile, the largest improvement is seen, as expected, for the silica or serpentine combinations (Figure 8). By adding these materials to our composite profile, we find that the requisite optical depth for olivine 1 drops slightly closer to $\tau_{10} = 0.20$ from $\tau_{10} = 0.24$. The aforementioned low optical depth of the silica and serpentine materials is closer to 0.02-0.03, and is consistent with zero. In all of our combinations, crystalline olivine remains the dominant constituent.

3.2.2. Impact of Data Treatment on Derived Peak Optical Depth

Additionally, we have examined whether choices made in the reduction and normalization of our PKS 1830-211 spectrum (§2) have impacted our derived optical depth estimates for the crystalline olivine 1 profile, for which we measured a peak optical depth of $\tau_{10} = 0.24 \pm 0.05$. First, we have explored whether our aggressive clipping of the noisy/discrepant data points has influenced our results, and we find that if we omit clipping, the peak optical depth rises to 0.27 ± 0.06 . We have then verified whether variations in the scaling factors used to join the SL and LL spectral orders, e.g. by excluding more points on the edges of the respective spectra and scaling the LL downwards by a larger factor, would impact our results, and we find that the peak optical depth shifts to 0.30 ± 0.05 . We have next explored whether variations in our quasar continuum normalization impact our results, and find peak optical depths which range from 0.24 ± 0.05 for the spline continuum to $0.29^{+0.06}_{-0.05}$ for the 4th order Chebyshev polynomial continuum. Finally, we elected not to spectrally-bin the final spectrum as in Kulkarni et al. (2007b, 2011), because while it improves the signal-to-noise ratio for individual data points, it also smooths over some of the finer spectral features. For comparison, utilizing the same methodology for normalizing by the quasar continuum, we would obtain a peak optical depth of $0.27^{+0.06}_{-0.05}$, if the spectrum were binned. All of these τ_{10} values, while generally slightly higher than our fiducial measurement, are consistent within $1\text{-}\sigma$ of that measurement. When an amorphous olivine profile was used in place of crystalline olivine in the tests, these statements are qualitatively unchanged, and we conclude that our results are robust to normalization and reduction variations.

3.3. Fits with Laboratory Amorphous Silicate Templates

In addition to examining laboratory crystalline silicates, we have considered profiles of laboratory amorphous silicates of olivine ($Mg_{2x}Fe_{2-2x}SiO_4$) and pyroxene ($Mg_xFe_{1-x}SiO_3$) compositions, where $0 < x < 1$ ¹. Previous studies of the $10\ \mu\text{m}$ silicate feature in DLAs (Kulkarni et al. 2007b, 2011) have determined that this absorption can generally be well explained by amorphous olivine. We find that amorphous olivines provide a better fit than amorphous pyroxenes, or than intermediate (not illustrated) amorphous silicate profiles, such as an amorphous version of the 21 Ferraro blend and an amorphous blend from Bowey & Adamson (2002). However, this amorphous olivine fit is still inferior to that produced by the crystalline silicate templates, and cannot reproduce the superimposed features within the broader $10\ \mu\text{m}$ silicate feature, without invoking absorption and emission mechanisms (§4).

We also explore, in the context of the amorphous olivine silicate profiles, the range in derived optical depths which can occur as a result of variations in the shapes of the dust particles and of the profile fitting range. Henning et al. (2005) and Molster & Kemper (2005) show that variations in grain size, shape, and metallicity can have an impact on the shape and peak-wavelength of the silicate profiles, as illustrated in Figures 6 and 7 of Chiar & Tielens (2006) for variations in the dust particles’ shapes, including solid versus porous particles, and solid glass versus a continuous distribution of ellipsoids. These differences are most pronounced in the $18\ \mu\text{m}$ region. We explore the impact of these variations by fitting three separate amorphous olivine profiles: one which is typical of solid spheres, one which is typical of a porous continuous distribution of ellipsoids, and one which is intermediate between these two extremes. These variations can produce optical depths with $0.11 \leq \tau_{10} \leq 0.13$, which while consistent within $1\text{-}\sigma$, serve to illustrate the

¹Throughout our analysis, we note that amorphous olivine/pyroxene refers to amorphous silicates of an olivine/pyroxene chemical composition, since intrinsically all olivines and pyroxenes are crystalline in structure (Henning 2010).

marked difference which slight variations in grain size and structure can have on the fit. The observed silicate feature is best fit by the intermediate amorphous olivine feature. We also note that the values of τ which are obtained fitting over the 10 μm region are consistent with those obtained over the extended fitting range for the amorphous olivine profiles. This suggests that our long-wavelength quasar continuum constraints are not unreasonable, although the relatively higher noise associated with the 18 μm data points, and the fact that we marginally cover the full extent of the 18 μm feature, places only weak constraints on the derived optical depth measurements.

3.3.1. *Crystalline and Amorphous Olivine in Combination*

We have also considered a bi-variate combination of amorphous and crystalline olivine in Table 5. As addressed in Bowey & Adamson (2002), the majority of analyses in both the local galaxy, and at higher redshift [e.g., Spoon et al. (2006)], have considered the 10 μm silicate feature to be produced primarily by an amorphous silicate, with residual structural features attributed to either crystalline silicates or to emission/absorption lines. In the case of the PKS 1830-211 absorber, however, the dominant constituent appears to be the crystalline silicate, since the addition of the amorphous olivine component neither significantly improves the χ_r^2 , nor is the optical depth of the amorphous olivine inconsistent with zero.

3.3.2. *Amorphous Olivine in Combination with SiC*

We have, additionally, examined a bi-variate combination of amorphous olivine with a profile feature attributed to SiC in a carbon AGB stellar spectrum. The results of this combination are shown in Table 5. Although SiC has not been found in abundance in the ISM, it is found in meteorites and in evolved stars and stellar products, including carbon stars, planetary nebulae, and some supernova remnants, e.g., Whittet et al. (1990); Speck et al. (1997); Stanghellini et al. (2007); Zijlstra et al. (2006); Yang et al. (2005); Gruendl et al. (2008); Bernard-Salas et al. (2009); Rho et al. (2010). We have, thus, considered the possibility that there is a broad amorphous olivine component, in addition to an absorption feature at 11.3 μm from SiC grains, producing the observed structure. We find, as illustrated in Figure 9, that adding SiC to the amorphous olivine improves the fit to the data, with the bulk of the optical depth being provided by the SiC component. Furthermore, the SiC component provides a relatively good fit to the feature in our spectrum near 11.3 μm . However, the combination of these two materials alone is not fully able to explain all of the observed structure in the spectrum of our quasar absorber. We also note in comparison, that while the addition of SiC improves the profile fit for amorphous olivine, it would make no improvement to the fit when combined with crystalline olivine material.

3.4. **Fits with Galactic Templates**

In addition to examining laboratory profiles in comparison with our PKS 1830-211 absorber spectrum, we also consider optical depth profiles derived from astrophysical sources within the Milky Way. These include measurements probing the diffuse ISM, dense molecular clouds or cloud complexes, young stellar objects (YSOs) embedded within molecular clouds, and circumstellar material. Kulkarni et al. (2011) have previously found that those DLA systems in which the 10 μm silicate feature is not fit by laboratory amorphous olivine, are instead well-fit by Galactic interstellar clouds, in which the dust is known to be composed of primarily

amorphous material (Kemper et al. 2004). They have not found any instances wherein dense molecular clouds provide the best fit. In our analysis of the PKS 1830-211 absorber, however, none of these Galactic profiles fit the 10 μm feature as well as the crystalline silicate profiles, largely because they do not exhibit significant structure within the 10 μm feature, and the peaks occur at lower wavelengths than in our data. In general, they also all produce inferior fits when compared with the best of the three amorphous olivine profiles. The best fit amongst the Galactic profiles is produced by a profile characteristic of AGB outflows, which is known from Molster & Kemper (2005) to be rich in crystalline silicates; this fit is only marginally worse than the laboratory amorphous olivine fit in terms of the χ_r^2 . Neither the molecular clouds, nor the diffuse ISM profiles produce a particularly good fit, and some of the molecular clouds, such as ρ Oph, characterized as a disturbed environment (Bowey et al. 2003), and the visually similar (not depicted) Serpens profile, produce significantly inferior fits when compared with, e.g., the Galactic center source profiles and those profiles for sources probing the the Taurus molecular cloud. Interestingly, profiles for sources embedded within the dense molecular clouds tend to produce slightly better fits than those illuminating the dark molecular clouds, which may stem from the fact that young embedded sources can be rich in crystalline silicates (Molster & Kemper 2005). We note that while not illustrated in our subset of 26 profiles, we have also considered profiles representative of comets, although the silicates in our PKS 1830-211 absorber are likely originating in a different environment. While these do exhibit structure similar to that in our system, they also generally peak at lower wavelengths, resulting in overall poor fits for the comet profiles considered.

3.5. Fits with ULIRG Templates

Finally, we examine a set of silicate optical depth profiles observed for UltraLuminous InfraRed Galaxies [ULIRGs; Spoon et al. (2006)]. These sources are dissimilar from our DLA host in the sense that they are undergoing intense star-formation, and so can be directly observed in emission even at high redshifts. In contrast, our DLA host is a late-type spiral which exhibits properties characteristic of other spiral galaxies at that redshift, based on its position on the Tully-Fisher relationship [see, e.g., Winn et al. (2002)]. However, ULIRGs do provide a comparative extragalactic source profile. They exhibit not only broad 10 and 18 μm silicate absorption features, but also a range of narrower emission and absorption features superposed over these broad silicate features. Even among the 12 ULIRGs studied by Spoon et al. (2006), there are visible differences between individual ULIRG profiles. Some, such as U4 (06301-7934), exhibit prominent emission features overlaying the broad silicate features, while in others such as U2 (00397-1312) these features are much weaker, or completely absent. We have, therefore, considered three different ULIRG profiles to encompass these variations. We find that while the ULIRG template fits are inferior to our crystalline silicate templates, they are better than both all of the examined Galactic sources and all of the laboratory amorphous profiles, likely because they exhibit more structure and generally peak at longer wavelengths. The fitted optical depths range for these ULIRG profiles from $0.12 \leq \tau_{10} \leq 0.15$ and $0.12 \leq \tau_{full} \leq 0.16$, which are self-consistent within 1- σ , although they are lower than the optical depths obtained for crystalline olivine. The presence of some of these prominent ULIRG emission and absorption features in our DLA host, in combination with broad amorphous olivine silicate absorption, could plausibly be used to provide an alternate origin for the structure in our PKS 1830-211 absorber spectrum, as discussed in §4.

4. DISCUSSION & CONCLUSIONS

In conclusion, based on our examination of a combined total of 92 observed and laboratory template profiles characterizing the 10 μm silicate absorption feature, of which we have focused on a representative subset of 26 profiles relative to the feature observed from the obscuring $z=0.886$ absorber towards PKS 1830-211, we have determined that our data are best fit by a laboratory crystalline olivine profile, possibly in combination with silica or serpentine materials. This finding is exceedingly unusual in the context of what is observed and known about silicates in other astrophysical sources. While crystalline silicates have been observed in a multitude of Galactic and extragalactic sources, they generally contribute $<15\%$ of the silicate mass, produce relatively narrow features, and when they are present, are predominant at longer wavelength IR bands and virtually absent or hidden near the 10 μm amorphous silicate feature. In the following section, we begin with a discussion of the plausibility of our finding of pure crystalline silicates in the PKS 1830-211 absorber, and then discuss several alternative scenarios which could potentially produce some of the observed structural features in the 10 μm region.

4.1. Crystalline Silicates

Our finding of pure, or nearly pure, crystalline silicates in the 10 μm region is atypical, given that the usually prominent broad 10 μm and 18 μm features are produced, either in emission or absorption, by the Si-O stretching and O-Si-O bending modes, respectively, of primarily amorphous silicate material. Although Bowey & Adamson (2002) have examined whether the broad 10 μm silicate feature could instead represent a superposition of numerous crystalline silicate features, Molster & Kemper (2005) deem this scenario unlikely given that the corresponding expected crystalline silicate resonances at longer wavelengths have not been observed. We discuss in the following subsections a comparison of the PKS 1830-211 quasar absorber crystallinity with other Galactic and extragalactic sources, and with other quasar absorption systems, and finally we discuss the physical environments for crystalline silicates.

4.1.1. Comparison With Other Astrophysical Sources

While such high crystallinity as we tentatively observe towards PKS 1830-211 is very rare, objects with some degree of crystalline silicates are ubiquitous both in the local universe, and at higher redshifts. Galactic objects with noted crystalline silicates include comets (7-90% crystallinity) Interplanetary Dust Particles (IDPs), primitive meteoritic materials, young stellar environments including pre-main sequence stars such as Herbig Ae/Be stars and T-Tau stars, and evolved stars, particularly those with oxygen- and dust-rich outflows such as (high mass loss) AGB stars (10-15% crystallinity), post-AGB stars, and Planetary Nebulae (Bouwman et al. 2003; Honda et al. 2003; Meeus et al. 2003; Molster & Kemper 2005; Uchida et al. 2004; Wooden et al. 1999). While a few rare stellar objects, such as the circumstellar disk around the peculiar carbon star IRAS 09425-6040, exhibit up to 75% crystallinity (Molster et al. 2001), the material around the more populous low mass stars is generally less crystalline-enriched; the winds of low mass post-MS stars exhibit $\leq 10\%$ crystallinity (Molster & Kemper 2005; Kemper et al. 2001). The diffuse ISM, at the lowest end of the spectrum, exhibits $\leq 2-5\%$ crystalline silicates (Kemper et al. 2004; Li et al. 2007). In the context of extragalactic sources, ULIRGs have been measured with at most 6-13% crystalline silicates (Spoon et al. 2006; Kemper et al. 2011), and these features are most pronounced longward of the 10 μm region. These ULIRG templates provide a better match to our spectrum than any of the other observational templates,

and we find that Galactic templates rich in crystalline silicates, such as AGB OH/IR outflows, produce a better fit to our data than crystalline-poor templates, such as those representing the diffuse ISM.

4.1.2. Comparison With Other Quasar Absorbers

Previous studies by our group of the silicate dust in other quasar absorbers have found no evidence for crystalline structure. Kulkarni et al. (2007b, 2011) examined 5 absorbers and found that the $10\ \mu\text{m}$ feature was best reproduced by templates from either laboratory amorphous silicates of an olivine composition, or by the primarily amorphous diffuse Galactic ISM templates. A visual examination of the amorphous silicate fits for these quasar absorption systems finds that there *are* weak residual structural features, which suggests that while the $10\ \mu\text{m}$ feature is primarily amorphous in composition, there are likely smaller contributions from crystalline silicates or from atomic/molecular features, as seen in the ULIRG profiles. These weak features are generally at lower wavelengths than those we are attributing to crystalline olivine. They did not consider a crystalline silicate template, however; so we have applied our expanded template set to their normalized data for four of these systems to investigate this possibility. We find that crystalline olivine produces a poor fit for all of their quasar absorption systems. Q0235+164 is best fit by the amorphous AmOlivGPC template, while Q0852+3435 is best fit by the AmOlivGS profile (see Table 3 for a description of these templates). The Q0937+5628 and 3C 196 quasar absorption systems are best fit by a profile typical of ULIRGs (ULIRG10), rather than by amorphous olivine, and in fact, 3C 196 is poorly fit by both amorphous and crystalline olivines. None of these quasar absorption systems exhibit the pronounced crystalline silicate features seen in the PKS 1830-211 spectrum, and the peaks of their $10\ \mu\text{m}$ absorption features are uniformly at lower wavelengths than in the PKS 1830-211 absorption system. Measurements of the spin temperatures in some of these systems, e.g. $T_s < 536\ \text{K}$ for Q0852+3435 (Srianand et al. 2008) and $T_s = 210\ \text{K}$ for Q0235+164 (Kanekar & Chengalur 2003), may be lower than that within the PKS 1830-211 system; Subrahmanyan et al. (1992) have noted an unusual, warm component in some of the H I material in the PKS 1830-211 $z=0.89$ absorber, with spin temperatures up to 1000 K. The primarily amorphous silicates in these other quasar absorption systems could be linked to their lower spin temperatures, although these temperatures are uncertain since they are linked to the covering factors.

4.1.3. Physical Conditions

If the features in our spectrum are indeed produced by crystalline silicates, it would be interesting to understand both the stimulus and physical environment producing these crystallines and whether they are similar to the crystalline silicates detected in more local systems. For instance, Galactic sources are observed to be generally Mg-rich and Fe-poor. Furthermore, Galactic crystalline silicates are found in a range of different temperature environments and may be formed through differing physical processes. Considering the relatively large value of R_V [6.34 ± 0.16 ; Falco et al. (1999)] estimated for the PKS 1830-211 absorber, which is suggestive of large grains associated with relatively dense regions, it is possible that the environment in the galaxy may be conducive to grain growth which could be linked with the apparent build-up of crystalline silicates detected. One should, however, note cautions by McGough et al. (2005) about the interpretation of R_V values in such lensed systems.

In light of the measurements of crystalline silicates in other astrophysical sources, and in the laboratory, there persist a number of puzzling questions for the $z=0.886$ absorption towards PKS 1830-211, if crystalline

silicates are invoked to explain the spectral structures. First, it is unclear why there is no evidence of amorphous silicates in the 10 μm region of the PKS 1830-211 absorption system. The dominance of amorphous silicates is well-illustrated by Figure 4 of Molster & Kemper (2005), which presents a collage of the spectra of Galactic objects in the 10 μm region; other than in comets, even those objects noted to be crystalline-rich exhibit a broad amorphous-type silicate profile with few pronounced crystalline features. Bouwman et al. (2003) demonstrate that this is because even in objects with noted high crystallinity, the amorphous silicates provide a much stronger relative contribution to the overall spectral energy distribution in the 10 μm region. In our spectrum, however, we see significant potential crystalline structure, which would imply an absence of the masking amorphous silicate material. It is not clear what mechanism would produce such a surfeit of crystalline material in the $z=0.886$ absorber towards PKS 1830-211, or alternatively, such a suppression of the amorphous silicates in the 10 μm region. Furthermore, in the 18 μm region, where crystalline silicates might be expected to be more prominently detected, our data are consistent with a broad amorphous-type structure with no distinctive crystalline features; however, we note that our visibly higher noise in this region could possibly obscure narrow crystalline signatures.

The second question which remains unclear is the temperature of the media producing and hosting the crystalline silicates. Temperature estimates within the $z=0.886$ absorber vary significantly according to Henkel et al. (2008), who estimate kinetic temperatures of ~ 80 K for 80-90% for the system, with warmer temperatures for the remaining 10-20% of the material, some of which is $\gtrsim 600$ K and generally concentrated in the spiral arm. Detailed studies of laboratory crystallines, in combination with observations of crystallines in Galactic sources, indicate that efficient production of crystallines requires temperatures in excess of ~ 1000 K, and that if the material cools too rapidly after formation then the material becomes quickly amorphized. However, since we are observing the silicate profile in *absorption* rather than emission, this suggests that the material may be relatively cool, although we note that, in principle, some warm material could also be detected in absorption. The detection of crystalline silicates in a cooler medium is not completely unusual; for instance cool meteorites exhibit significant quantities of crystalline silicates. The presence of such cool crystalline silicates in an extragalactic environment would suggest that the crystalline material may have been transported in, e.g., a cooling outflow from an initially hotter medium; in ULIRGs, the cooling outflows stemming from evolved stars within the star-bursts are invoked to explain the temperature discrepancy between the observed crystalline silicate absorption and the required high temperature formation medium. Alternatively, Molster et al. (1999) have found evidence that the cooler, lower-density, disk-like material in some evolved stars exhibits a high abundance of crystalline silicates at temperatures below the annealing temperatures, and have attributed their existence to an unidentified low-temperature crystallization process. Laboratory experiments have indicated that partial crystallization can be achieved at room temperature through electron irradiation, although it is unclear whether this process is effective in astrophysical environments (Carrez et al. 2001).

The third aspect which remains unclear is the iron content in the material. In addition to constraining the species and derived expected behavior of the quasar absorber dust material, the iron content can be used for comparisons of the Fe/Si ratio in the dust with Fe/Si ratios inferred indirectly from gas phase depletions in other systems. For instance, Welty et al. (2001) have illustrated that along some sight lines in the SMC, Fe exhibits severe depletion while Si can exhibit much milder depletions than would be expected from the depletions of other refractory species, in contrast with what is observed for the Milky Way. Galactic crystalline silicates are generally Mg-rich and Fe-poor, although some large ($>1\mu\text{m}$ diameter) crystalline silicates with Fe are found in the solar system (Molster et al. 2002). However, DLAs (Prochaska et al. 2007; Kulkarni et al. 2010) generally show significant Fe-depletions, so their dust grains are unlikely to be completely Fe-poor. An assessment of longer wavelength IR spectral data is required to establish the relative

Fe-enrichment in this source, as described in §5.

Finally, there remain a number of alternatives for the formation mechanism of the crystalline silicates within the PKS 1830-211 absorption system. In general Galactic crystallines are believed to form via one of three primary mechanisms: (i) gas phase condensation about the glass temperature, which is thought to be the primary mechanism around evolved stars; (ii) annealing (crystallization via heating), or formation following melting, of amorphous grains in a high temperature environment, which is the primary mechanism invoked in the accretion disks of young stars; or (iii) formation as a by-product of planet-formation mechanisms, as invoked for comets, such as through the collisional cascade of asteroid-sized objects due to gravitational effects, or through flash-heating by shocks stimulated by protoplanet-disk tidal interactions (Molster & Kemper 2005; Molster et al. 2002; Bouwman et al. 2003; Harker & Desch 2002). Although these mechanisms can successfully produce sizable quantities of crystalline silicates, these crystallines are rapidly amorphized by a range of mechanisms including sputtering, evaporation, cosmic-rays, grain-grain collisions, supernova shock waves and adsorption of Fe (Molster & Kemper 2005; Molster et al. 2002; Tielens et al. 1998). In the ISM, crystallines may be amorphized within either <10 Myr (Kemper et al. 2004) or 70 Myr (Bringa et al. 2007) timescales by heavy ion cosmic rays, depending on the model.

In the case of ULIRGs, the relatively high crystallinity may be explained by enhanced ongoing star-formation. Spoon et al. (2006) ascribe the high percentage of crystallines to recent merger-triggered star-formation, and postulate that the amorphization process lags the injection of dust which is driven by the intense star-formation. They posit that this crystalline-rich dust is originating in evolved massive stars, such as red supergiants, luminous blue variables, and Type II supernovae. Numerical simulations in Kemper et al. (2011), however, suggest that even under the assumption of intense star-formation rates ($1000 M_{\odot} \text{ yr}^{-1}$) and highly efficient dust production by supernovae, they are barely able to explain the 6.5-13% crystallinity observed in ULIRGs, and with more realistic, lower, values for these rates, the addition of a secondary heating source, such as an AGN, is required to fully explain the observed crystallinity.

The scenarios which appear the most probable to explain the observed crystalline silicates in the PKS 1830-211 absorption system run a wide gamut. (i) The first scenario is an extreme burst of star-formation within the SW spiral arm, which is heavily obscured by both dust and molecular material. Alternatively, one of the PKS 1830-211 lines of sight could trace a path directly through an isolated, high stellar mass cluster in which strong outflows have transported the crystalline silicates into a slightly cooler region, in which the crystalline material have not yet amorphized. While intense star-formation has been invoked to explain the crystallinity in ULIRGs, there is no evidence for intense star-formation within the spiral arms of the PKS 1830-211 absorber galaxy. However, the SW arm is noted to be significantly rich in molecules, suggesting some enrichment mechanism. We do note that while Muller et al. (2006) have found isotopic ratios ($^{17}\text{O}/^{18}\text{O}$, $^{14}\text{N}/^{15}\text{N}$, and $^{32}\text{S}/^{34}\text{S}$) for this absorber which differ from those in the Milky Way, and R_V is relatively high (Falco et al. 1999), there is also evidence that the dust-to-gas ratio in this system is consistent with the Galactic value (Dai et al. 2006). (ii) The second scenario is intense, recent, AGN activity which produced outflows to export crystalline silicates from the central torus, or a strong flux of UV radiation to anneal the amorphous silicates, as has been invoked by Kemper et al. (2011) to help explain the ULIRG crystallinity. However, there is no published evidence of a strong AGN in the absorber galaxy. (iii) The crystalline material could have been abundantly produced in young stellar disks, instead of in evolved stellar outflows. However, in this scenario, the material should be hotter, and potentially detected in emission, rather than absorption. Furthermore, this mechanism would again require a massive (undetected) starburst to produce adequate quantities of crystalline silicates to dominate the profile. (iv) The remaining mechanism which could be invoked is that of shock-heated material, perhaps from a localized, extreme shock resulting from a transient

event. Shock-heating mechanisms have been used to explain the crystalline silicates in comets (Harker & Desch 2002), although we note that very strong shocks could destroy not only the crystalline structure but also the dust grains themselves. The origin of the shocking mechanism in the absorbing galaxy remains unclear, however, and detailed simulations would be required to determine whether a large scale shock could produce sufficient temperatures to form the crystalline structures without destroying the dust grains. We regard scenario (i) as the most likely given the high molecular content and large R_V value of the absorber.

4.2. Amorphous Silicate Absorption Combined with Atomic/Molecular Features

While we believe that crystalline silicates provide a simpler explanation for the observed structure, we now explore a variety of scenarios to assess whether the observed features could be reproduced without crystalline silicates. As an alternative potential explanation for the observed structure within the 10 μm silicate feature, we investigate whether it could be a combination of a broad absorption feature produced by an amorphous silicate of olivine composition and a series of additional atomic and molecular absorption/emission features within the DLA material. This possibility is worth exploring because (i) the 10 μm amorphous silicate feature is present in many Galactic and extragalactic sources; (ii) this absorption system is rich in molecular material, as indicated by observed sub-mm transitions (Wilkind & Combes 1996, 1998); (iii) narrow absorption and emission features have been observed in ULIRGs (Spoon et al. 2006); and (iv) previous detections of crystalline silicates in astrophysical sources, e.g. ULIRGs, have been much weaker than in our profile.

We have implemented a series of fits utilizing our three amorphous olivine templates from Table 3, and manually masking what appear to be potential superposed absorption/emission features. We have considered one mask with emission features at 9.3-10.05 μm and 10.35-10.85 μm , termed mask A, and a second mask (termed B) which has these emission features in addition to an absorption feature at 10.85-11.3 μm . We fit these masked profiles to our spectrum both as described in §3.1, and using an alternative algorithm which allows the template profile to be uniformly shifted in wavelength to produce the best fit. We permit the wavelength-shifting because (i) as discussed in §3.1 variations in silicate grain morphology can produce marked offsets in the peak of the optical depth profile; and (ii) recent work by R. Nikutta (private communication) suggests that sizable wavelength shifts in the 10 μm peak can be produced around quasars with a clumpy dust torus model which combines simultaneous silicate detections in absorption and emission, in conjunction with the rising quasar continuum. Although we are not looking at dust within a quasar torus, this work raises the possibility that clumpy dust in which some material is seen in emission, while other dust is seen in absorption, could contribute to the observed wavelength offsets. The results of our fits are presented in Table 6 and in Figures 10 and 11. We find that using maskB, with or without shifting, we can obtain fits formally equal to, or better than, those from the crystalline silicate templates. However, while formally improved based on the χ_r^2 values, there are many fewer points which are being directly fitted within the deepest part of the optical depth profile, and the bulk of the fitting leverage is being applied by the wings. We have also explored utilizing a reduced fitting range spanning 8.0-12.3 μm to minimize the leverage from these regions, but find this produces a negligible difference in the resulting fits, and an increase in the χ_r^2 reflecting the reduced number of fitted points. Thus, given the reduced number of sample points being fit, we do not consider the masked fits as reliable as those in our primary analysis.

Furthermore, the masking scenario is contingent upon all of the identified emission and absorption features being physically explicable by molecular and atomic transitions. In order to determine whether there are plausible atomic and molecular lines which could produce these features, we have considered prominent

lines which are seen in other extragalactic and Galactic sources (see Figure 12). An emission feature in the 9.3-10.05 μm region could possibly arise from the 9.66 μm H_2 S(3) molecular transition which is prominently observed in some ULIRGs (Spoon et al. 2006; Higdon et al. 2006). However, the emission feature that we would need to mimic the structure seen in our 10 μm profile appears both much broader and slightly offset to lower wavelengths relative to the ULIRG H_2 feature (see Figure 4). Also, if the potential emission feature is due to H_2 S(3), then the corresponding H_2 S(1) feature at 17.0 μm should also be detected, and while there is weak evidence of an emission feature in this region, our data are too noisy to conclusively argue for its presence. The emission feature from 10.35-10.85 μm could possibly be explained by the [S IV] 10.51 μm feature, which is also observed in some ULIRGS, although our feature appears stronger than that seen in the Spoon et al. (2006) ULIRGs. Finally, the \sim 10.85-11.3 μm masked absorption feature is consistent in location with the weak 11 μm crystalline silicate feature observed in some ULIRGs (Spoon et al. 2006); if crystalline silicates are only needed to explain part of the overall shape of our 10 μm absorption profile, then we could claim a much smaller degree of overall silicate crystallinity in this system.

Although absorption and emission features detected in other astrophysical sources are detected at approximately the correct wavelengths to explain the structure in the PKS 1830-211 spectrum, without invoking crystalline silicates, there is no strong evidence that all of these particular features can be physically produced and detected. Emission lines of H_2 and S [IV] are detected in ULIRGs, but these objects are undergoing extreme star-formation, and can be detected in emission. By contrast, the PKS 1830-211 DLA host is a regular spiral which is barely detected in HST images, with no noted pronounced star-formation. It seems unlikely that strong emission lines of these species would be produced in such an environment. Furthermore, it is unclear whether the emission features in ULIRGs are of appropriate line strengths and line widths to explain the features in our spectrum. In order to investigate this, we have produced two modified ULIRG profiles (U4N and U10N) which exclude the prominent PAH emission features between 11-12 μm , which we do not detect, but which retain the remaining emission features in the 10 μm region. If similar transitions are producing these features in ULIRGs and in our DLA host galaxy, then these features should align. We illustrate the fit to the U4N profile, which has the most pronounced features, in Figure 13 and find that globally the H_2 and S [IV] emission features, and the 11 μm crystalline absorption feature occur at approximately the correct wavelengths. However, these emission features are broader in our quasar absorption system than in the ULIRGs, suggesting they may be line-blends, or incorrect identifications. Furthermore, while equivalent width measurements of the H_2 line in U4N and in our system may be comparable, the emission line in the ULIRG U4N was the most pronounced of the ULIRG sample, and the H_2 feature in a more representative ULIRG will not be of adequate strength to explain the emission required in our system.

In addition to considering mask A and mask B in our fitting scenarios, we have also considered two other masks which exclude the 8.65-9.25 μm spectral region. These masks could plausibly explain the data if there was an ammonia absorption feature in this region. Mask C includes an absorption feature at 8.65-9.25 μm and an emission feature at 10.35-10.85 μm , while mask D retains these features as well as an additional absorption feature from 10.85-11.3 μm . While molecular studies have found indications of ammonia in the absorber system, and the silicate profiles of some Galactic sources (Kwok 2007; Zasowski et al. 2008; Gibb et al. 2000) exhibit absorption from ammonia, these two masks do not fit the data as well as mask A or mask B, and so we discount this scenario.

4.3. Foreground Galaxy Absorption

An alternative scenario to explain the structure in the PKS 1830-211 absorber spectrum is that we are detecting superposed amorphous silicate features from two different sources, which are absorbed at different wavelengths, spectrally combining to produce the appearance of multi-peaked structure. This is plausible in that a $z=0.19$ foreground galaxy (Lovell et al. 1996) is located within 10 kpc of the NE quasar sightline, and so our spectrum is also probing the material in the outskirts of this $z=0.19$ foreground galaxy, which may contain silicate dust. If we perform a bi-variate fit in which we consider an amorphous olivine template at the rest-frame of our $z=0.886$ quasar-absorption-host, combined with an amorphous olivine template at the rest-frame of the $z=0.19$ galaxy, as in Appendix A.2, we do not find this to be viable, however. At the wavelength at which we would expect $10 \mu\text{m}$ silicate absorption in the $z=0.19$ foreground galaxy, we instead detect an emission-type feature. We, therefore, conclude that the structure in the $10 \mu\text{m}$ region of the PKS 1830-211 absorber spectrum is not the superposition of $10 \mu\text{m}$ silicate absorption from the DLA host galaxy and $18 \mu\text{m}$ silicate absorption from the $z=0.19$ foreground galaxy.

We have also repeated the bi-variate fitting allowing for a foreground galaxy at any arbitrary redshift. This scenario covers the possibility in which a dark object which is rich in silicate material was missed in previous studies, as well as covering the possibility that the $z=0.19$ galaxy might in fact be at a higher redshift closer to the $z=0.886$ galaxy, as suggested by Lehár (2000), or that the $z=0.886$ galaxy might in fact be multiple galaxies, as proposed by Courbin et al. (2002). However, we do not find any such “hidden” object responsible for producing superposed silicate absorption features in our spectrum.

4.4. Amorphous Silicates with Superposed Emission

Finally, we consider that the PKS 1830-211 spectrum could be produced by foreground or coeval emission superposed upon a broad amorphous olivine silicate feature. For instance, we could be detecting broad silicate absorption along the SW quasar line of sight probing the molecule-rich material, while simultaneously be detecting emission from, e.g. crystalline silicates, along the other quasar line of sight. Alternatively, if the presumed $z=0.19$ galaxy is instead a massive galaxy located at $z=0.886$, as proposed by Lehár (2000), or the $z=0.886$ host galaxy is instead comprised of two neighboring galaxies, as proposed by Courbin et al. (2002), then we might expect a blend of silicate absorption with either some limited emission or absorption reflecting a differing chemical composition, from the second galaxy. This latter scenario has largely been excluded by the bi-variate fitting tests in §3.2, in which we did not find compelling evidence arguing for two distinct chemical compositions, although we cannot exclude a weak contribution from a second source. In the former case of absorption and emission, the broad amorphous silicate absorption would still need to be offset in wavelength to fit our spectrum, as would the crystalline silicate emission template. Furthermore, while we can reproduce emission features of approximately the correct width on top of the broad absorption feature to explain the structure, with wavelength offsets, no single offset or explored crystalline silicate could simultaneously reproduce all of the observed peaks/substructure. Additionally, as in the case of invoking atomic and molecular emission lines, it is not clear that such emission should be detectable from the $z=0.886$ host galaxy, or any companion galaxies.

Alternatively, some of the foreground emission could be produced by a transient object within our own Galaxy or solar system, perhaps connected to the scattered light feature discussed in Appendix A.1. At the rest frame of the $z=0.886$ absorber, the flux from a foreground object would be probing a slightly longer wavelength region than the $z=0.886$ absorber, where crystalline silicate resonances would be more abundant.

For instance, Bouwman et al. (2010) find abundant crystalline silicates around a young M4 dwarf with a proto-planetary disk, and as discussed in §A.2, there is an M4 dwarf within our slit. However, we do not believe that this particular star contributes significantly to our PKS 1830-211 absorption spectrum, nor is it believed to be a particularly young stellar system, and so any crystalline silicates produced during its youth are expected to have dissipated. Furthermore, the likelihood of a transient source providing significant crystalline structure seems unlikely, and as discussed in Appendix A.1, we do not expect contamination from the scattered light feature to be strong enough to produce structure at the level we observe in the PKS 1830-211 spectrum.

5. SUMMARY

In summary, based on an infrared spectrum of PKS 1830-211 obtained with the Spitzer IRS, we have detected the presence of a 10 μm silicate absorption feature at a $>10\text{-}\sigma$ significance level, as well as the presence of an 18 μm silicate absorption feature. This reinforces previous findings from Kulkarni et al. (2007b, 2011) that silicate material is a component of DLA dust. We have found that the 10 μm silicate feature is best fit by crystalline olivine, possibly in combination with a second material such as silica and serpentine. Given the rarity of such high-crystalline silicate dust, we have explored a variety of other scenarios invoking atomic and molecular absorption/emission lines, and a combination of silicate dust in two foreground absorbers; but none of these alternative scenarios satisfactorily reproduce the observed structure in the PKS 1830-211 spectrum.

In order to confirm the presence of the postulated crystalline silicates, and to eliminate some of these suggested formation scenarios, supplemental data are required. In particular, longer-wavelength moderately high resolution mid-IR and far-IR data ($> 20\mu\text{m}$ in the $z=0.889$ absorber rest frame) are needed to provide evidence for the presence of longer wavelength crystalline resonances and to constrain the relative amount of Fe present in the system. As discussed in Molster & Kemper (2005), the 69 μm forsterite band has been used in evolved stars to provide evidence of the high Mg/Fe ratio, as the band shifts to longer wavelengths as more Fe is introduced into the silicate. Furthermore, this band can provide constraints on the temperature of the material, as addressed by Bowey et al. (2002). Data spanning a broader spectral range could also provide evidence to support/rule out other atomic, PAH, and molecular transitions in both the quasar and the absorber which have been discussed as possible candidates for producing the additional structure we see in our spectrum, within and outside of the 10 μm silicate feature. Higher resolution spectra covering the 10 μm and 18 μm spectral regions could also be of great use for ascertaining better estimates of the structure and line widths, which in turn could help discriminate between the emission/absorption scenario and the crystalline silicate scenario. These data would also help rule out any contributions to the spectra from the anomalous scattered light feature (Appendix A.1), as it is believed to result from a transient source, and so should be absent in follow-up observations. Finally, spectroscopic or photometric observational constraints on the amount of star-formation within the obscured SW spiral arm of the $z=0.886$ absorbing galaxy could help to further constrain the formation mechanisms of the silicate dust.

We thank the Spitzer Science Center help desk for their assistance with the IRS data analysis and interpretation of the scattered light feature. We also acknowledge use of several subroutines taken from Press et al. (1992) which were used in our analysis. This work is based on observations made with the Spitzer Space Telescope, and has made use of the NASA/ IPAC Infrared Science Archive, which are operated by the Jet Propulsion Laboratory, California Institute of Technology under a contract with the National Aeronautics

and Space Administration (NASA). Support for this work is provided by NASA through an award issued by JPL/Caltech: Spitzer grant PID-50783 (PI V. P. Kulkarni). Additional support comes from National Science Foundation grant AST-0908890 to the Univ. of South Carolina (PI V. P. Kulkarni).

Facilities: Spitzer (IRS).

A. Minor Caveats

We note the presence of two distinct spectral contaminants, one physical and one spurious, which impact our data but which we believe do not significantly alter our conclusions.

A.1. Scattered Light Feature

First, we have identified an anomalous emission feature in our 2-D LL spectra which we associate with scattered light. The relatively broad feature is adjacent to our quasar spectrum at approximately $(\alpha, \delta) = (18:33:36, -21:03:41.3)$ in each of our LL1, LL2, and LL3 spectra. The centroid of this feature is approximately 8 pixels away from the quasar spectrum at the wavelength relevant to our 10 μm absorption feature. This prominent anomalous feature exhibits a spatially narrower distribution at low LL wavelengths, which broadens progressively as the wavelength increases; at the longest LL1 wavelengths it appears to be bifurcated with the light generally concentrated in two spatially distinct prongs, and a diffuse contribution in-between. Thus, while at the lowest LL wavelengths we do not believe this feature substantially contributes to our spectrum, at the longest wavelengths it visibly crosses through our narrow PKS 1830-211 spectrum.

We have determined that the origin of this feature is most likely scattered light, from a bright off-field object. A visual inspection of both ground-based and HST visible and near-IR data reveals no significant objects at the spatial location of the feature. Furthermore, we have utilized *SPICE* to extract the spectrum of this feature, and compared it with a catalog of known stellar spectra observed with the Spitzer IRS (Ardila et al. 2010), and with quasar spectra; the feature does not match any of these spectral shapes. The Spitzer Science Center help desk has confirmed that this feature is in all probability a very rare scattered light feature, of unidentified origin, although the most likely candidates are either an IR bright source near the galactic plane, or a transitory object from our own solar system. Neither we, nor the help desk, could find any bright optical or IR sources in the immediate vicinity of our target. We have also ruled out detector features, such as latents or bad dark corrections, as the origin of this feature.

As this scattered light feature is spatially broad, and visibly crosses through the quasar spectrum at the longest wavelengths, it may be the origin of the observed discrepancies between the two LL1 nod positions in the 22-26 μm spectral region. This location corresponds to the 11.7-13.8 μm region in the rest frame of the $z=0.886$ absorber. As discussed in §2.2, a discrepancy on the order of 15-20%, in which one nod position exhibits a broad emission-type feature while the other exhibits a broad absorption-type feature, is present over this spectral range. In order to identify the origin of this discrepancy, which is larger than those observed in the SL and LL2 spectral orders, we have first examined the position of the slit-centering to determine whether perhaps an offset in centering is causing a foreground/background object to fall within the slit for one of the nod positions, but not for the other. However, the header information indicates that there are variations of at most $(\Delta\alpha, \Delta\delta) = (0.''018, 0.''009)$ and $(0.''020, 0.''014)$ within the two nod positions, and no significant offsets (within one pixel) in-between the nod positions; IRS exhibits pointing uncertainties

on the order of $1''$ (which is smaller than the pixel scale). There is no evidence to suggest that we have a slight pointing mismatch, which could result in the inclusion of extra flux from a foreground/background object in only some of the exposures, nods, or orders.

We have also explored whether the difference between the two nod positions could stem from the background subtraction. As we were unable to subtract the background by differencing the two nod positions because of the anomalous scattered light feature, we have instead constructed a background generated from the combined off-source LL2 images. It is plausible that a background gradient, independent from the scattered light feature, might be contaminating one nod background or region of the chip but not the other. In order to check this, we have utilized *SPICE* to extract a background spectrum from both multiple locations across our LL2 background image, as well as across a region of each of the LL1 spectra not covered by the quasar or the scattered light feature. We do not detect any substantial variations between the intrinsic backgrounds in the two nod positions, nor do we detect any significant spatial variations in the subtracted background, indicative of either a gradient or of a region of slightly bad pixels underlying one of the nod positions. We have also confirmed that the feature is not a result of any treatment of the background by the extraction algorithm, by replacing the pixels within the scattered light feature of the 2D spectrum with representative background pixels, and repeating the extractions; the extracted structural features remain unchanged. An additional test using the IRAF task *apall* confirms that treatment of the background in our extraction algorithm is not the origin of the derived structure.

Additionally, we have explored whether the difference in the 22-26 μm spectral region could stem from a localized event along one of the spectra, such as an isolated cosmic ray burst or transitory event. In order to test this, we have extracted the combined 20-exposure spectrum, for each nod, as well as four subset spectra with 5 exposures each. We find that all of the spectral features in each nod position, including the discrepancy, are virtually identical between these five extractions. Therefore, it is unlikely that an isolated transitory event produced the discrepancy.

Thus, the most likely explanation for the discrepancy in the 22-26 μm region is contamination from the scattered light feature, which peaks in intensity over this 4 μm region, and more strongly affects one of the nod positions than the other. An inspection of the 2-dimensional spectrum shows that the scattered light feature is both the most narrow and has the highest surface brightness at the short wavelength end of LL1, where it is well-separated (~ 8 pixels) from the quasar spectrum. As the wavelength increases, the breadth of this feature also increases. However, the potential impact of this increased contamination at the longest wavelengths is mitigated by the decrease in surface brightness of the feature with increasing wavelength. In order to determine whether a narrower extraction window might minimize this contribution, we have compared a *SPICE* extraction obtained using the default point-source extraction template, which is of variable spatial width becoming broader at longer wavelengths, with two manual template extractions, one of which is 3 pixels wide, and one of which is 5 pixels wide. Modifying the extraction template impacts the absolute calibration of the extracted spectrum, but as we are only utilizing the manual extractions to compare features within the spectrum, this is not an issue. While we do find that the continuum level is slightly different between the extractions, as expected, we find no significant differences in the shape of the PKS 1830-211 spectrum or in any of the spectral features, along either nod position. Thus, employing a narrower extraction template would not change our analysis. We also have no method by which to separate any possible contamination occurring directly over the location of the quasar spectrum from the quasar spectrum itself, as this scattered light feature does not exhibit any standard spectral type. We, thus, rely on the combination of the two nod positions to effectively cancel out the contamination pattern within this 22-26 μm region, with resultant larger uncertainties associated with the data points.

A.2. Contamination from Foreground Objects

The second contaminant of our quasar absorption system spectrum comes from several foreground objects which are also present within the slit. However, none of these objects seem to be bright enough to affect our analysis, as we describe below. As discussed briefly in §2.1, in addition to the two images of the lensed quasar and the $z=0.886$ quasar absorber host galaxy within the slit, a foreground star and a lower-redshift foreground galaxy are also encompassed by the IRS slit in all spectral orders. The brighter of the two quasar sight lines, termed the NE or A component in the literature, is located at 18h33m39.931s and $-21^{\circ}03'39.''75$, while the dimmer, and more dust-obscured quasar sightline to the SW is located at $(\Delta\alpha, \Delta\delta) = (-0.''64, -0.''73)$ from the NE component (Winn et al. 2002). The host galaxy for the absorber, which has been identified as an Sb/Sc spiral, is separated by $(\Delta\alpha, \Delta\delta) = (-0.''33, -0.''49)$ from the NE quasar component (Winn et al. 2002). The absorber subtends a physical scale of 7.6 kpc'', assuming $H_0=73$ km s $^{-1}$ Mpc $^{-1}$ and a standard Λ CDM cosmology. Our requested central slit position of 18h33m39.89s, -21d03m40.4s places it close to the center of this quasar absorption system.

The foreground star which is also present within the slit, termed S1 in the literature, dominates the combined light distribution at optical wavelengths, but has a minimal impact at the mid-IR wavelengths under consideration in this analysis. This star, which is located at $(\Delta\alpha, \Delta\delta) = (0.''09, 0.''53)$ relative to the NE quasar component, has been identified as a likely M4 dwarf star by Courbin et al. (2002) and Djorgovski (1992). Star S1 dominates the total light at visible wavelengths, contributing between 57-74% of the total light at F555W (V) and 68-83% of the total light at F814W (I), based on the magnitudes for the star and other objects within the slit provided by Winn et al. (2002) and Courbin et al. (2002); differences in the total contribution by S1 reflect variations in separating the light contributed by different objects by these authors. In the near-infrared, however, S1 contributes a much smaller percentage of the total light: 38-44% at F160W (H) and 20-23% at F205W (K) (Lehár 2000; Courbin et al. 2002). Extrapolating these rapidly decreasing relative contributions to the spectral region covered by the IRS, we would expect close to 1% of the total flux to be contributed by S1 at the shortest ($5\mu\text{m}$) wavelengths covered, and less than 0.01% at the longest wavelengths covered. These findings of a negligible contribution to the total flux are reconfirmed by rescaling the IRS spectra for three brighter early M dwarf stars (HD180617, GJ687, and GJ849) provided in the compilation of IRS stellar spectra by Ardila et al. (2010); we find $\approx 0.5\%$ contribution to the total flux near $5\mu\text{m}$, and 0.001% contribution to the total flux near $35\mu\text{m}$. In the region where the $z=0.886$ quasar absorber $10\mu\text{m}$ silicate feature is located, we find only an 0.01% contribution to the spectrum by these rescaled, similar stars from the Spectral Atlas. The small contribution of the M4 dwarf to our combined spectrum is a result of the rapidly decreasing strength of the stellar emission at mid-IR wavelengths, with the increasing strength of the underlying quasar continuum flux density. Furthermore, we have verified through an inspection of the HD180617 stellar spectrum that we do not expect any significant structural features to be produced in our spectrum from an M4 dwarf star. We, thus, exclude the possibility that the spectral features we see in the PKS 1830-211 spectrum are produced by this foreground star.

The second potential foreground contaminant to our quasar spectrum is the $z=0.19$ (Lovell et al. 1996; Wilkind & Combes 1998; Courbin et al. 2002; Winn et al. 2002) galaxy, termed G2 in the literature, which also lies within the slit, and is separated by $(\Delta\alpha, \Delta\delta) = (0.''24, -2.''49)$ from the NE quasar component. We do not believe that this galaxy will produce a significant contribution for three reasons. First, it is substantially ($\Delta m_{F205W} = 3.35\text{mag}$) fainter than the NE quasar sightline in the near-infrared, and is less reddened than the quasar (Lehár 2000). Hence, any mid-IR emission produced by the galaxy should be negligible. Second, any spectral features contributed by the galaxy will be well-separated spectrally from those of the 0.886 quasar absorber host galaxy. Third, the central regions of the foreground galaxy are not

being directly illuminated by either of the quasar sight lines, and so material from the foreground galaxy should not be producing significant absorption in the quasar spectrum. However, the closer, NE quasar line of sight passes within 10 kpc of the center of this foreground galaxy (assuming a standard Λ CDM cosmology with $H_0=73 \text{ km s}^{-1} \text{ Mpc}^{-1}$) and so may be probing the outer regions of this $z=0.19$ foreground galaxy. Thus, in order to confirm that none of the prominent features which we observe coincide with silicate absorption in a $z=0.19$ galaxy, we have shifted the intermediate amorphous olivine profile (AmOliv) into the rest frame of the $z=0.19$ galaxy and repeated our fitting procedure. As illustrated in Figure 14, we find that while the purported $10 \mu\text{m}$ feature could be explained by $18 \mu\text{m}$ silicate absorption in the $z=0.19$ foreground galaxy, there is no corresponding $10 \mu\text{m}$ absorption feature for this foreground galaxy. At the wavelength at which we would expect to detect $10 \mu\text{m}$ silicate absorption in the $z=0.19$ foreground galaxy there is a weak emission feature detected instead. We, therefore, conclude that the structure we see in the PKS 1830-211 spectrum does not originate from a superposition of $10 \mu\text{m}$ absorption from the DLA and $18 \mu\text{m}$ absorption from the $z=0.19$ foreground galaxy.

The deblending of the objects in this field, based on their HST WFPC2 and NICMOS images, remains uncertain, and it is possible that there are further additional objects contained within the slit. Courbin et al. (2002); Meylan et al. (2005) and Lehár (2000) have identified a second foreground star, termed star P, located at $(\Delta\alpha, \Delta\delta) = (-0.''3, -0.''5)$ relative to the NE quasar component; Winn et al. (2002) have instead argued that this object is the bulge of the $z=0.886$ galaxy, and the current photometry is unable to distinguish between the two scenarios. Given that this object is 0.02-0.04 times fainter than star S1 at F205W, it would not have a significant impact on the derived profile should it indeed be a foreground star. Furthermore, Courbin et al. (2002) argue that the object considered to be a single $z=0.886$ galaxy by Winn et al. (2002), may in fact be comprised of two galaxies near $z=0.89$, one of which exhibits significant spiral features. The impact of two companion galaxies is addressed briefly in §4, in which we have searched for simultaneous absorption, or simultaneous emission and absorption, at arbitrary redshifts in order to explain the observed spectral features. However, this explanation does not adequately account for the spectral structure which we observe, which indicates that if two galaxies are contributing to the observed silicate absorption profile, they either have a similar chemical composition and redshift, or one of the objects is dominating the absorption profile.

REFERENCES

- Aguirre, A. N. 1999a, ApJ, 512, L19
- Aguirre, A. 1999b, ApJ, 525, 583
- Ardila, D. R. et al. 2010, ApJS, 191, 301
- Barger, A. J., Cowie, L. L., Sanders, D. B., Fulton, E., Taniguchi, Y., Sato, Y., Kawara, K., & Okuda, H. 1998, Nature, 394, 248
- Bernard-Salas, J., Peeters, E., Sloan, G. C., Gutenkunst, S., Matsuura, M., Tielens, A. G. G. M., Zijlstra, A. A., & Houck, J. R. 2009, ApJ, 699, 1541
- Bernstein, R. A., Freedman, W. L., & Madore, B. F. 2002, ApJ, 571, 107
- Boissé, P., Le Brun, V., Bergeron, J., & Deharveng, J.-M. 1998, A&A, 333, 841
- Bottinelli, S. et al. 2009, ApJ, 690, L130

- Bouwman, J., de Koter, A., Dominik, C., & Waters, L. B. F. M. 2003, *A&A*, 401, 577
- Bouwman, J., Lawson, W. A., Juhász, A., Dominik, G., Feigelson, E. D., Henning, Th., Tielens, A. G. G. M., & Waters, L. B. F. M. 2010, *ApJ*, 723, 243
- Bowey, J. E. & Adamson, A. J. 2001, *MNRAS*, 320, 131
- Bowey, J. E. & Adamson, A. J. 2002, *MNRAS*, 334, 94
- Bowey, J. E. et al. 2002, *MNRAS*, 331, L1
- Bowey, J. E., Adamson, A. J., & Yates, J. A. 2003, *MNRAS*, 340, 1173
- Bringa, E. M. et al. 2007, *ApJ*, 662, 372
- Calzetti, D., Armus, L., Bohlin, R. C., Kinney, A. L., Koornneef, J., & Storchi-Bergmann, T. 2000, *ApJ*, 533, 682
- Campins, H. & Ryan, E. V. 1989, *ApJ*, 341, 1059
- Carrez, P., Demyk, K., Leroux, H., & Cordier, P. 2001, *M&PSA*, 36, 36
- Chary, R., & Elbaz, D. 2001, *ApJ*, 556, 562
- Chengalur, J. N., de Bruyn, A. G., & Narasimha, D. 1999, *A&A*, 343, L79
- Chiar, J. E. & Tielens, A. G. G. M. 2006, *ApJ*, 637, 774
- Chiar, J. E. et al. 2011, *ApJ*, 731, 9
- Courbin, F., Meylan, G., Kneib, J.-P., & Lidman, C. 2002, *ApJ*, 575, 95
- Dai, X., Kochanek, C. S., Chartas, G., & Mathur, S. 2006, *ApJ*, 637, 53
- Djorgovski, S. et al. 1992, *MNRAS*, 257, 240
- Elbaz, D., Aussel, H., Cesarsky, C. J., Desert, F. X., Fadda, D., Franceschini, A., Harwit, M., Puget, J. L., & Starck, J. L. 1998, *The Universe as seen by ISO*, eds. P. Cox and M. F. Kessler (UNESCO, Paris, ESA Special Publications Series)
- Falco, E. E. et al. 1999, *ApJ*, 523, 617
- Fall, S. M., & Pei, Y. C. 1993, *ApJ*, 402, 479
- Ferraro, J. R. 1892, *The Stadler Infrared Spectra Handbook of Minerals and Clays* (Stadler Research Laboratories)
- Frye, B., Welch, W. J., & Broadhurst, T. 1997, *ApJ*, 478, L25
- Gibb, E. L. et al. 2000, *ApJ*, 536, 347
- Gordon, K. D., Clayton, G. C., Misselt, K. A., Landolt, A. U., Wolff, M. J. 2003, *ApJ*, 594, 279
- Gruendl, R. A., Chu, Y.-H., Seale, J. P., Matsuura, M., Speck, A. K., Sloan, G. C., & Looney, L. W. 2008, *ApJ*, 688, L9

- Hao, L., Weedman, D. W., Spoon, H. W. W., Marshall, J. A., Levenson, N. A., Elitzur, M., & Houck, J. R. 2007, *ApJ*, 655, L77
- Harker, D. E., & Desch, S. J. 2002, *ApJ*, 565, 109
- Henkel, C., Braatz, J. A., Menten, K. M., & Ott, J. 2008, *A&A*, 485, 451
- Henkel, C. et al. 2009, *A&A*, 500, 725
- Henning, T., Mutschke, H., & Jäger, C. 2005, *IAUS*, 231, 457
- Henning, T. 2010, *ARA&A*, 48, 21
- Higdon, S. J. U., Armus, L., Higdon, J. L., Soifer, B. T., & Spoon, H. W. W. 2006, *ApJ*, 648, 323
- Honda, M., Kataza, H., Okamoto, Y. K., Miyata, T., Yamashita, T., Sako, S., Takubo, S., & Onaka, T. 2003, *ApJ*, 585, L59
- Houck, J. R. et al. 2004, *ApJS*, 154, 18
- Kanekar, N., & Chengalur, J. N. 2003, *A&A*, 399, 857
- Kemper, F., Waters, L. B. F. M., de Koter, A., & Tielens, A. G. G. M. 2001, *A&A*, 369, 132
- Kemper, F., Vriend, W. J., & Tielens, A. G. G. M. 2004, *ApJ*, 609, 826
- Kemper, F., Markwick, A. J., & Woods, P. M. 2011, *MNRAS*, 413, 1192
- Knez, C. et al. 2005, *ApJ*, 635, L145
- Koopmans, L. V. E., & de Bruyn, A. G. 2005, *MNRAS*, 306, L6
- Kulkarni, V. P., Fall, S. M., Lauroesch, J. T., York, D. G., Welty, D. E., Khare, P., & Truran, J. W. 2005, *ApJ*, 618, 68
- Kulkarni, V. P., Khare, P., Péroux, C., York, D. G., Lauroesch, J. T., & Meiring, J. D. 2007a, *ApJ*, 661, 88
- Kulkarni, V. P., York, D. G., Vladilo, G., & Welty, D. E. 2007b, *ApJ*, 663, L81
- Kulkarni, V. P., Khare, P., Som, D., Meiring, J., York, D. G., Péroux, C., & Lauroesch, J. T. 2010, *New A Rev.*, 15, 735
- Kulkarni, V. P., Torres-Garcia, L. M., Som, D., York, D. G., Welty, D. E., & Vladilo, G. 2011, *ApJ*, 726, 14
- Kwok, S. 2007, *Physics and Chemistry of the Interstellar Medium* (Sausalito, CA: University Science Books)
- Lehár, J. et al. 2000, *ApJ*, 536, 584
- Li, M. P., Zhao, G., Li, A. 2007, *MNRAS*, 382, L26
- Lovell, J. E. J. et al. 1996, *ApJ*, 472, L5
- Madau, P., Ferguson, H. C., Dickinson, M. E., Giavalisco, M., Steidel, C. C., & Fruchter, A. 1996, *MNRAS*, 283, 1388
- McGough, C., Clayton, G. C., Gordon, K. D., & Wolff, M. J. 2005, *ApJ*, 624, 118

- Meeus, G., Sterzik, M., Bouwman, J., & Natta, A. 2003, *A&A*, 409, L25
- Molster, F. J. et al. 1999, *Nature*, 401, 563
- Menten, K. M., Güsten, R., Leurini, S., Thorwirth, S., Henkel, C., Klein, B., Carilli, C. L., & Reid, M. J. 2008, *A&A*, 492, 725
- Meylan, G., Courbin, F., Lidman, C., Kneib, J.-P., & Tacconi-Garman, L. E. 2005, *A&A*, 438, L37
- Molster, F. J., Yamamura, I., Waters, L. B. F., Nyman, L.-Å., Käuffl, H.-U., de Jong, T., & Loup, C. 2001, *A&A*, 366, 923
- Molster, F.J., Bradley, J. P., & Sitko, M. L. 2002, *LPI*, 33, 1471
- Moster, F., & Kemper, C. 2005, *Space Sci. Rev.*, 119, 3
- Muller, S., Guélin, M., Dumke, M., Lucas, R., & Combes, F. 2006, *A&A*, 458, 417
- Muller, S., & Guélin, M. 2008, *A&A*, 491, 739
- Ostriker, J. P., Vogeley, M. S., & York, D. G. 1990, *ApJ*, 364, 405
- Papovich, C., Dickinson, M., & Ferguson, H. C. 2001, *ApJ*, 559, 620
- Pei, Y. C., Fall, S. M., & Bechtold, J. 1991, *ApJ*, 378, 6
- Pei, Y. C. 1992, *ApJ*, 395, 130
- Pei, Y. C., Fall, S. M., & Hauser, M. G. 1999, *ApJ*, 522, 604
- Péroux, C., Kulkarni, V. P., Meiring, J., Ferlet, R., Khare, P., Lauroesch, J. T., Vladilo, G., & York, D. G. 2006, *A&A*, 450, 53
- Péroux, C., Bouché, N., Kulkarni, V. P., York, D. G., & Vladilo, G. 2011, *MNRAS*, 410, 2237
- Pettini, M., Smith, L. J., Hunstead, R. W., & King, D. L. 1994, *ApJ*, 426, 79
- Pettini, M., Smith, L. J., King, D. L., & Hunstead, R. W. 1997, *ApJ*, 486, 665
- Press, W. H., Teukolsky, S. A., Vetterlig, W. T., & Flannery, B. P. 1992, *Numerical Recipes in Fortran 77: The Art of Scientific Computing*, Vol. 1 (2nd ed.; New York, NY: Cambridge University Press)
- Prochaska, J. X., Gawiser, E., Wolfe, A. M., Castro, S., & Djorgovski, S. G. 2003, *ApJ*, 595, L9
- Prochaska, J. X., O'Meara, J. M., Herbert-Fort, S., Burles, S., Prochter, G. E., & Bernstein, R. A. 2006, *ApJ*, 648, L97
- Prochaska, J. X., Wolfe, A. M., Howk, J., Gawiser, E., Burles, S. M., & Cooke, J. 2007, *ApJS*, 171, 29
- Rho, J., Gomez, H., Lagage, P.-O., Boogert, A., Reach, W. T., & Dowell, D. 2010, *cosp*, 38, 2824
- Riess, A. G. et al. 2004, *ApJ*, 607, 665
- Roche, P. F., & Aitken, D. K. 1984, *MNRAS*, 208, 481
- Sembach, K. R., & Savage, B. D. 1992, *ApJS*, 83, 147

- Shapley, A. E., Steidel, C. C., Adelberger, K. L., Dickinson, M., Giavalisco, M., & Pettini, M. 2001, *ApJ*, 562, 95
- Sofia, U. J., Gordon, K. D., Clayton, G. C., Misselt, K., Wolff, M. J., Cox, N. L. J., & Ehrenfreund, P. 2006, *ApJ*, 636, 753
- Somerville, R. S., Primack, J. R., & Faber, S. M. 2001, *MNRAS*, 320, 504
- Speck, A. K., Barlow, M. J., & Skinner, C. J. 1997, *M&PS*, 32, 703
- Spoon, H. W. W. et al. 2006, *ApJ*638, 759
- Srianand, R., Gupta, N., Petitjean, P., Noterdaeme, P., & Saikia, D. J. 2008, *MNRAS*, 391, L69
- Stanghellini, L., García-Lario, P., Garca-Hernández, D. A., Perea-Calderón, J. V., Davies, J. E., Manchado, A., Villaver, E., & Shaw, R. A. 2007, *ApJ*, 671, 1669
- Storrie-Lombardi, L. J., & Wolfe, A. M. 2000, *ApJ*, 543, 552
- Subrahmanyam, R., Kesteven, M. J., & te Lintel Hekkert, P. 1992, *MNRAS*, 259, 63
- Tielens, A. G. G. M., Waters, L. B. F. M., Molster, F. J., & Justtanont, K. 1998, *Ap&SS*, 255, 415
- Uchida, K. I. et al. 2004, *ApJS*, 154, 439
- van Breemen, J. M. 2011, *A&A*, 526, A152
- Vladilo, G., & Péroux, C. 2005, *A&A*, 444, 461
- Welty, D. E., Lauroesch, J. T., Blades, J. C., Hobbs, L. M., & York, D. G. 2001, *ApJ*, 554, L75
- Werner, M. W. et al. 2004, *ApJS*, 154, 1
- Whittet, D. C. B., Duley, W. W., & Martin, P. G. 1990, *MNRAS*, 244, 427
- Wiklind, T., & Combes, F. 1998, *ApJ*, 500, 129
- Wiklind, T., & Combes, F. 1996, *Nature*, 379, 139
- Winn, J. N., Kochanek, C. S., McLeod, B. A., Falco, E. E., Impey, C. D., & Hans-Walter Rix, H.-W. 2002, *ApJ*, 575, 103
- Wooden, D. H., Harker, D. E., Woodward, C. E., Butner, H. M., Koike, C., Witteborn, F. C., & McMurtry, C. W. 1999, *ApJ*, 517, 1034
- Wolfe, A. M., Lanzetta, K. M., Foltz, C. B., & Chaffee, F. H. 1995, *ApJ*, 454, 698
- Yang, X., Chen, P., & He, J. 2004, *A&A*, 414, 1049
- York, D. G., et al. 2006, *MNRAS*, 367, 945
- Zasowski, G., Kemper, F., Watson, Dan M., Furlan, E., Bohac, C. J., Hull, C., & Green, J. D. 2009, *ApJ*, 694, 459
- Zijlstra, A. A. et al. 2006, *MNRAS*, 370, 1961

Table 1. PKS 1830-211 Spitzer IRS Observations

Order	λ -Coverage	t_{exp} (s)	N_{exp}	$t_{obs}(m)$
SL2	5.13-7.60	60	19	38
SL1	7.46-14.29	60	20	40
LL2	13.90-21.27	120	10	40
LL1	19.91-39.90	120	20	80

Note. — Summary of Spitzer IRS observations. In the first column we list the spectral order, followed by the wavelength coverage (in μm), the exposure time per frame, the number of exposures, and the total on-target exposure for the spectral order in minutes. This total time is double $t_{exp}N_{exp}$, because of the two nod positions.

Table 2. Template Summary: Observed Profiles from Literature

Profile	λ_{peak}	$\lambda_{min} - \lambda_{max}$	Ref	Description
EXTRAGALACTIC SOURCES: ULIRGS				
U2	10.17	7.80 - 32.38	1	ULIRG 00397-1312
U4	10.11	7.95 - 32.84	1	ULIRG 06301-7934
U10	10.32	8.40 - 33.70	1	ULIRG 18443+7433
U4N	10.11	7.95 - 32.84	1	ULIRG 06301-7934 (excl 11-12 μm features)
U10N	10.32	8.40 - 33.70	1	ULIRG 18443+7433 (excl 11-12 μm features)
DIFFUSE ISM				
GCS	9.64	7.54 - 34.83	1	galactic center source GCS-3
WR118	9.78	7.51 - 12.94	2	WC Wolf-Rayet star (WR118)
DENSE MOLECULAR CLOUD/CLOUD COMPLEX				
E116 ^a	9.54	8.09 - 12.84	3	Star (Elias 16) behind Taurus
Q21-6	9.70	5.58 - 13.88	4	Q21-6 - Star (G8.5 IIIa Fe-0.5) behind IC 5146
Trap	9.64	8.09 - 12.82	5	Trapezium region of Orion nebula
ρ Op	9.75	7.50 - 12.21	6	SSTc2d_J163346.2-242753 star behind ρ Ophiuchi
T-TAURI STAR EMBEDDED IN MOLECULAR CLOUD				
E17	9.37	8.08 - 12.78	7	Elias 7N (K5V) in Taurus
E129	9.47	8.33 - 13.33	7	Elias 29 in ρ -Oph
STELLAR MATERIAL				
μ Cep	9.69	8.00 - 13.50	8	μ Cephei red supergiant
AGB	10.08	7.05 - 29.90	7	OH/IR 127.8+0.0 (AGB outflows)
SiC(star)	11.25	8.83 - 12.66	9	AFGL 3068 (carbon AGB star with SiC in absorption)

^asmoothed profile from Bowey & Adamson (2002)

Note. — Summary of 15 optical depth profile templates extracted from the literature for observed, astrophysical, sources. In the first column we list our abbreviated name, followed by the peak wavelength for the 10 μm silicate feature, the range of wavelengths spanned by the profile, the literature reference, and finally a description of the profile. All wavelengths are specified in μm . For broad profiles with significant structure, such as the ULIRGs, the deepest, not necessarily central, wavelength is listed as the peak. REFS: (1) Spoon et al. (2006); (2) Chiar & Tielens (2006); (3) Bowey & Adamson (2002); (4) Chiar et al. (2011); (5) Bowey & Adamson (2001); (6) van Breemen (2011); (7) Bowey et al. (2003); (8) Roche & Aitken (1984), & (9) Speck et al. (1997)

Table 3. Template Summary: Laboratory Profiles from Literature

Profile	λ_{peak}	$\lambda_{min} - \lambda_{max}$	Ref	Description
LABORATORY - Amorphous				
AmOlivGS	9.89	8.34 - 29.75	1	Amorphous olivine glass (solid sphere)
AmOlivGPC	9.81	7.54 - 27.63	1	Amorphous olivine glass (porous CDE ^a)
AmOliv	9.73	7.66 - 34.95	2	Amorphous olivine
AmPyrGPC	9.06	7.09 - 27.65	1	Amorphous pyroxene glass (porous CDE ^a)
LABORATORY - Crystalline				
Cry21Fer	9.21; 9.86	7.79 - 13.24	3	Crystalline 21 Ferraro mixture
CryPyr	9.33; 9.86	7.76 - 13.33	3	Crystalline pyroxene mixture
CrySerp	9.26; 10.20	7.70 - 13.25	3	Crystalline serpentine mixture
CrySil	9.21; 12.63	7.81 - 13.33	3	Crystalline silica mixture
CryOliv1	10.27; 11.25	7.81 - 13.23	3	Crystalline olivine (1)
CryOliv2	10.00; 11.12	7.84 - 13.26	3	Crystalline olivine (2)

^acontinuous distribution of ellipsoids, as opposed to spherical particles.

Note. — As in Table 2, but listing 10 optical depth profiles for laboratory sources extracted from the literature as follows: (1) Chiar & Tielens (2006); (2) Spoon et al. (2006); & (3) Bowey & Adamson (2002). All amorphous olivines and pyroxenes are technically amorphous silicates of an olivine/pyroxene chemical composition (Henning 2010).

Table 4. Optical Depth Fits for PKS 1830-211 Absorber

Profile	τ_{10}	$\chi_{r,10}^2$	Fit λ_{range}	τ_{full}	$\chi_{r,full}^2$	Fit λ_{range}
EXTRAGALACTIC SOURCES: ULIRGS						
U2	0.12±0.03	9.04	8.00-13.30	0.13±0.04	7.43	8.00-19.45
U4	0.12±0.03	10.50	8.00-13.30	0.12±0.03	8.13	8.00-19.45
U10	0.15±0.03	8.86	8.40-13.30	0.16±0.04	6.99	8.40-19.45
U4N	0.12±0.03	8.45	8.00-13.30	0.12±0.03	6.97	8.00-19.45
U10N	0.15±0.03	8.86	8.40-13.30	0.16±0.04	6.99	8.40-19.45
DIFFUSE ISM						
GCS	0.12±0.03	13.54	8.00-13.30	0.13±0.04	10.18	8.00-19.45
WR118	0.12±0.03	14.18	8.00-12.94	0.12±0.03	14.18	8.00-12.94
DENSE MOLECULAR CLOUD						
EL16	0.10±0.03	14.30	8.09-12.84	0.10±0.03	14.30	8.09-12.84
Q21-6	0.11±0.03	12.34	8.00-13.30	0.11±0.03	11.57	8.00-13.88
Trap	0.10±0.02	13.72	8.09-12.82	0.10±0.02	13.72	8.09-12.82
ρ Op	0.10±0.03	17.38	8.00-12.20	0.10±0.03	17.38	8.00-12.20
YSO EMBEDDED IN MOLECULAR CLOUD						
El7	0.10±0.03	14.13	8.09-12.78	0.10±0.03	14.13	8.09-12.78
El29	0.12±0.03	13.30	8.33-13.30	0.12±0.03	13.30	8.33-13.31
STELLAR MATERIAL						
μ Cep	0.12±0.03	12.75	8.00-13.25	0.12±0.03	12.75	8.00-13.25
AGB	0.11±0.03	11.56	8.00-13.30	0.11±0.03	8.44	8.00-19.45
SiC	0.27±0.05	10.05	8.83-12.66	0.27±0.05	10.05	8.83-12.66
LABORATORY - AMORPHOUS						
AmOlivGS	0.13±0.03	12.24	8.34-13.30	0.13±0.04	8.40	8.34-19.45
AmOlivGPC	0.12±0.03	11.35	8.00-13.30	0.12±0.03	8.11	8.00-19.45
AmOliv	0.12±0.03	11.27	8.00-13.30	0.13±0.04	8.07	8.00-19.45
AmPyrGPC	0.09±0.03	15.73	8.00-13.30	0.10±0.03	11.40	8.00-19.45
LABORATORY - CRYSTALLINE						
Cry21Fer	0.11±0.03	14.79	8.00-13.24	0.11±0.03	14.79	8.00-13.24
CryPyr	0.10±0.03	12.96	8.00-13.30	0.10±0.03	12.96	8.00-13.33
CrySerp	0.14±0.04	13.30	8.00-13.23	0.14±0.04	13.30	8.00-13.23
CrySil	0.09±0.04	23.84	8.00-13.26	0.09±0.04	23.84	8.00-13.26
CryOliv1	0.24±0.05	5.70	8.00-13.23	0.24±0.05	5.70	8.00-13.23
CryOliv2	0.26±0.06	7.44	8.00-13.26	0.26±0.06	7.44	8.00-13.26

Note. — Best fits for each of our 26 optical depth template profiles. In the first column we list the profile name, followed by the peak optical depth normalization factor (a_n , here termed τ), the reduced chi-squared, and the wavelength range over which the fit was performed. All wavelengths are in μm . Columns 2-4 correspond to fitting over solely the 10 μm feature (8.0-13.3 μm), while columns 5-7 correspond to fits extended to cover the maximum wavelength encompassed by the PKS 1830-211 spectrum, if profile data are available, or to the maximum wavelength covered by the profile if it is not.

Table 5. Two-Mineral Fitting of the 10 μm Feature

Profile1	Profile2	τ_1	τ_2	χ_r^2	Fit λ_{range}
Cry. Olivine1	Silica	0.23 \pm 0.05	0.02 \pm 0.04 ^a	5.34	8.00 - 13.23
Cry. Olivine1	Serpentine	0.21 \pm 0.05	0.03 \pm 0.04 ^a	5.43	8.00 - 13.23
Cry. Olivine1	Pyroxene	0.23 \pm 0.05	0.01 \pm 0.03 ^a	5.62	8.00 - 13.23
Cry. Olivine1	Ferraro21	0.22 \pm 0.05	0.02 \pm 0.03 ^a	5.56	8.00 - 13.23
Cry. Olivine1	Amorph Olivine	0.22 \pm 0.05	0.01 \pm 0.03 ^a	5.63	8.00 - 13.23
Cry. Olivine1	SiC star	0.24 \pm 0.05	0.01 \pm 0.05 ^{a,b}	5.27	8.83 - 12.66
Am. Olivine	SiC star	0.06 \pm 0.03	0.18 \pm 0.05	6.30	8.83 - 12.66

^a1- σ limit formally extends below 0.0; lower limit is considered to be effectively 0.

^bSiC τ value is at the lowest boundary explored in the calculation, $\tau = 0.005$ and is consistent with zero. We, thus, discount this fit, regardless of the low χ_r^2 .

Note. — Fits resulting from bi-variate ($\exp(-(a_n\tau_{1,norm} + b_n\tau_{2,norm}))$) profile combinations, with nomenclature as detailed for Table 4. All wavelengths are in μm . Olivine 1, which produced the lowest χ_r^2 in Table 4 is used for the first profile in every combination but the last. The best fit is the olivine1 + silica, although it is only a marginal improvement over the pure olivine 1fit.

Table 6. Amorphous Olivine Profiles with PKS 1830-211 Masking

Profile	τ_{10}	χ_r^2	Fit λ_{range}	$\Delta\lambda$	τ_{full}	χ_r^2	Fit λ_{range}	$\Delta\lambda$
LABORATORY - AMORPHOUS - AmOliv								
fiducial	0.12 \pm 0.03	11.27	8.00-13.30	0.000	0.13 \pm 0.03	8.07	8.00 - 19.45	0.000
maskA	0.19 \pm 0.04	7.23	8.00-13.30	0.000	0.16 \pm 0.04	5.96	8.00 - 19.45	0.000
maskB	0.16 \pm 0.04	4.89	8.00-13.30	0.000	0.15 \pm 0.04	4.44	8.00 - 19.45	0.000
maskA	0.24 \pm 0.05	3.81	8.00-13.30	0.300	0.19 \pm 0.05	4.89	8.00 - 19.45	0.275
maskB	0.21 \pm 0.05	3.26	8.00-13.30	0.250	0.16 \pm 0.05	4.02	8.00 - 19.45	0.200
LABORATORY - AMORPHOUS - AmOlivGPC								
fiducial	0.12 \pm 0.03	11.35	8.00-13.30	0.000	0.12 \pm 0.03	8.11	8.00 - 19.45	0.000
maskA	0.16 \pm 0.04	9.12	8.00-13.30	0.000	0.15 \pm 0.04	6.64	8.00 - 19.45	0.000
maskB	0.14 \pm 0.04	6.18	8.00-13.30	0.000	0.13 \pm 0.04	4.92	8.00 - 19.45	0.000
maskA	0.23 \pm 0.05	3.41	8.00-13.30	0.400	0.18 \pm 0.05	4.67	8.00 - 19.45	0.450
maskB	0.21 \pm 0.05	3.18	8.00-13.30	0.400	0.16 \pm 0.05	4.10	8.00 - 19.45	0.325
LABORATORY - AMORPHOUS - AmOlivGS								
fiducial	0.13 \pm 0.03	12.24	8.34-13.30	0.000	0.13 \pm 0.04	8.40	8.34 - 19.45	0.000
maskA	0.22 \pm 0.04	6.84	8.34-13.30	0.000	0.19 \pm 0.05	5.78	8.34 - 19.45	0.000
maskB	0.19 \pm 0.04	3.44	8.34-13.30	0.000	0.17 \pm 0.05	3.82	8.34 - 19.45	0.000
maskA	0.27 \pm 0.05	2.51	8.62-13.30	0.275	0.19 \pm 0.05	4.44	9.27 - 19.45	0.925
maskB	0.24 \pm 0.05	1.27	8.59-13.30	0.250	0.18 \pm 0.05	3.45	8.52 - 19.45	0.175

Note. — Optical depth profile fits from three amorphous olivine templates, showing the fiducial fits (from Table 4), as well as fits employing masking of the presumed absorption/emission features in the PKS 1830-211 spectrum, and simultaneous masking and shifting of the template profile, in order to obtain the best fit. Two broad fitting regions are tabulated: 8.0-13.30 μm and 8.0-19.45 μm , with the fitting region adjusted as appropriate to ensure template coverage. The nomenclature is as in Table 4, with the wavelengths in μm . The masks are applied to cover the following spectral regions: A (9.3-10.05 μm ; 10.35-10.85 μm) and B (9.3-10.05 μm ; 10.35-11.3 μm). The best fits occur for the maskB + shifting fits - but these are also weakly constrained in the 10 μm region and assume that the requisite emission/absorption features are produced by plausible physical mechanisms.

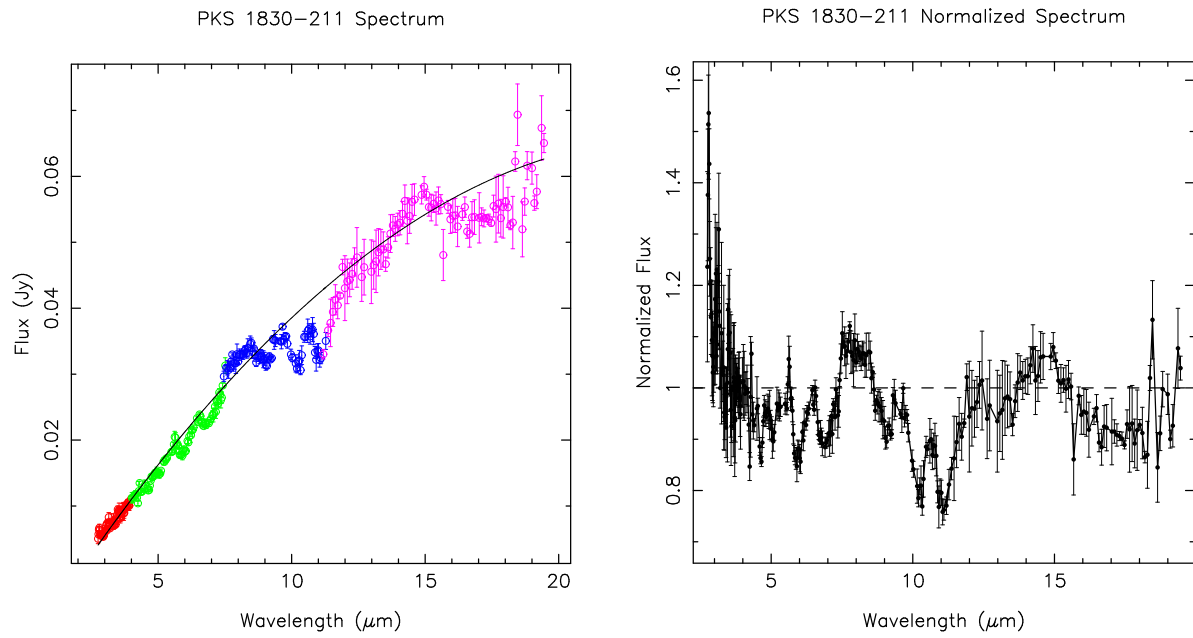


Fig. 1.— PKS 1830-211 spectrum. Left: Observed flux versus absorber rest-frame ($z=0.886$) wavelength with the colors denoting individual spectral orders as follows: red-SL2; green-SL1; blue-LL2; and magenta-LL1. The black line depicts the 3rd order Chebyshev polynomial fit to the quasar continuum used to normalize the spectrum. Right: The resultant normalized spectrum, as a function of absorber-rest-frame wavelength, with the dashed line denoting unity.

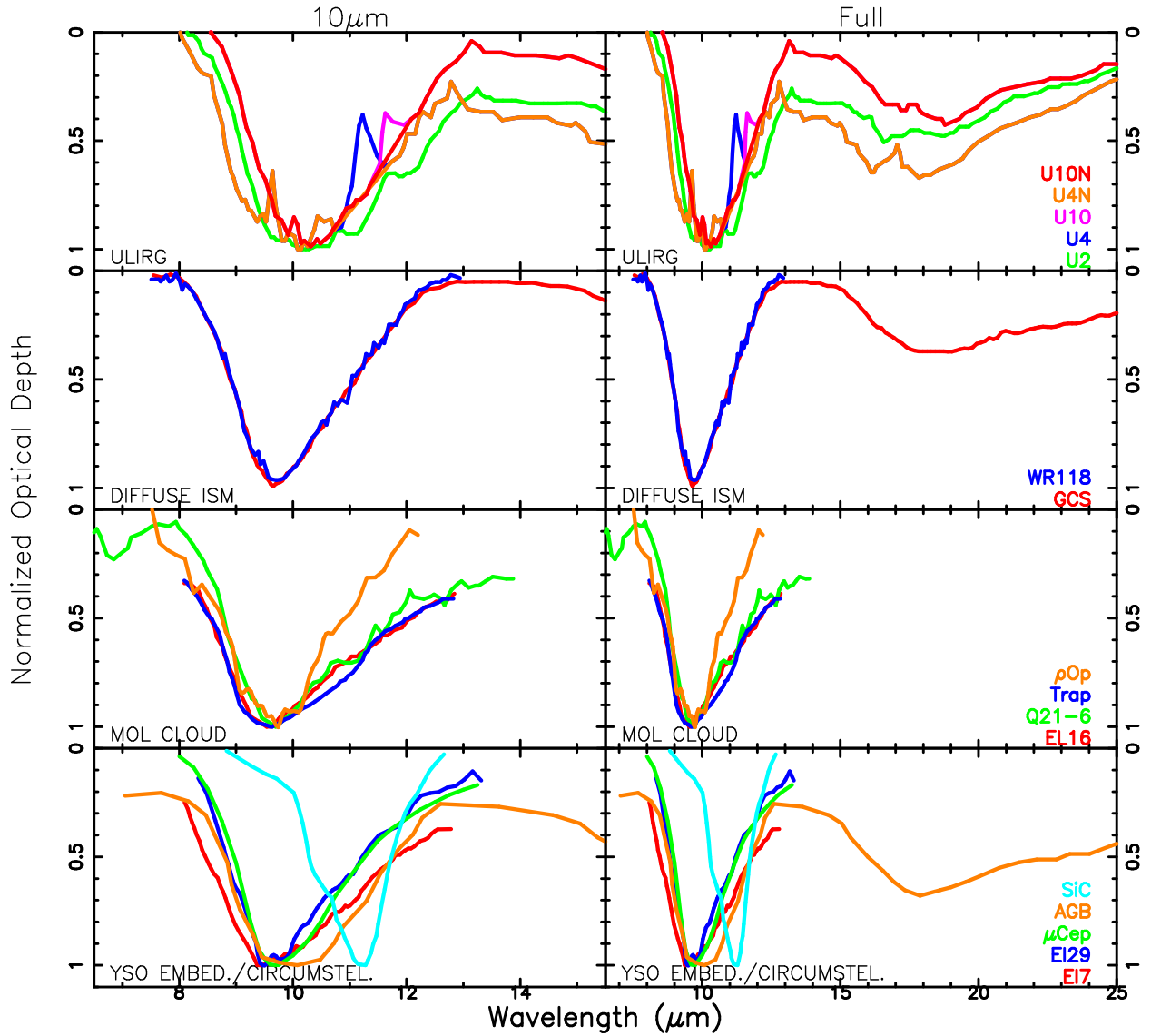


Fig. 2.— Optical depth template profiles for observed (astrophysical) sources drawn from the literature, as detailed in Table 2, sorted by category, and split into different panels for clarity. The left column depicts the profile over the 10 μm silicate feature. The right column depicts the profile over the extended fitting region including the 18 μm silicate feature, if available.

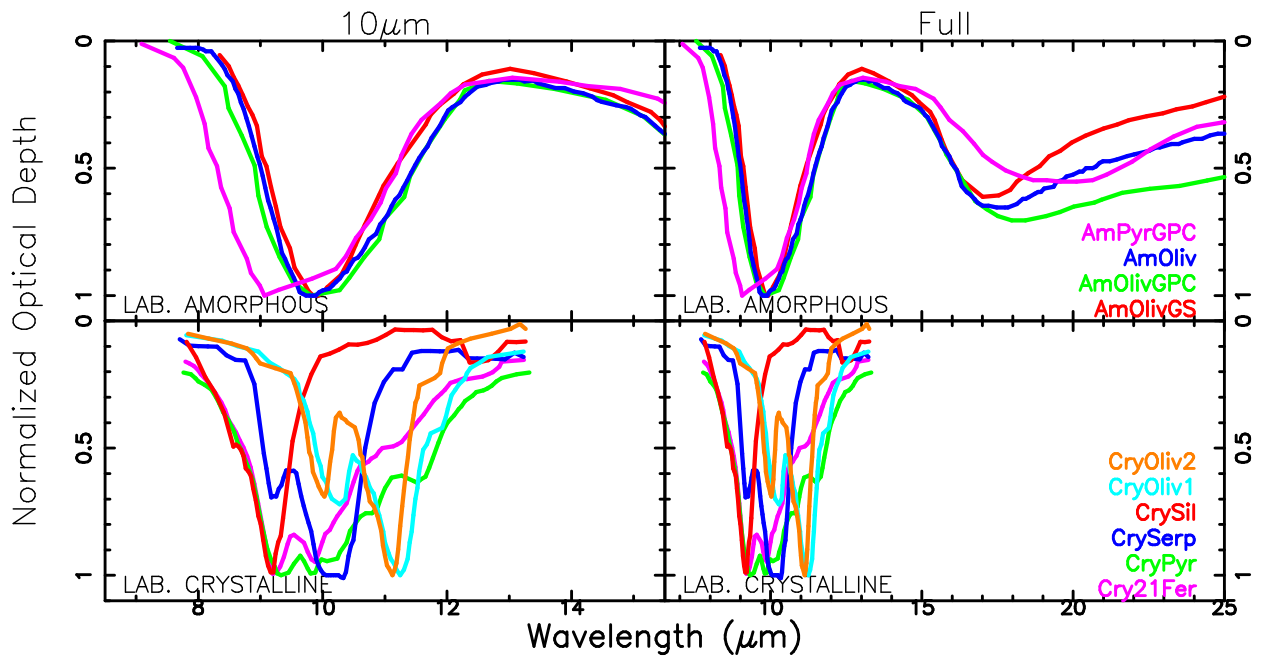


Fig. 3.— Similar to Figure 2, but for the laboratory profiles (Table 3) drawn from the literature. Note the complex structure for the crystalline silicate profiles, in contrast with the the relatively featureless amorphous profiles. Variations in grain shape and size can have a visible impact on the shape of the profiles, as illustrated by the three amorphous olivine templates.

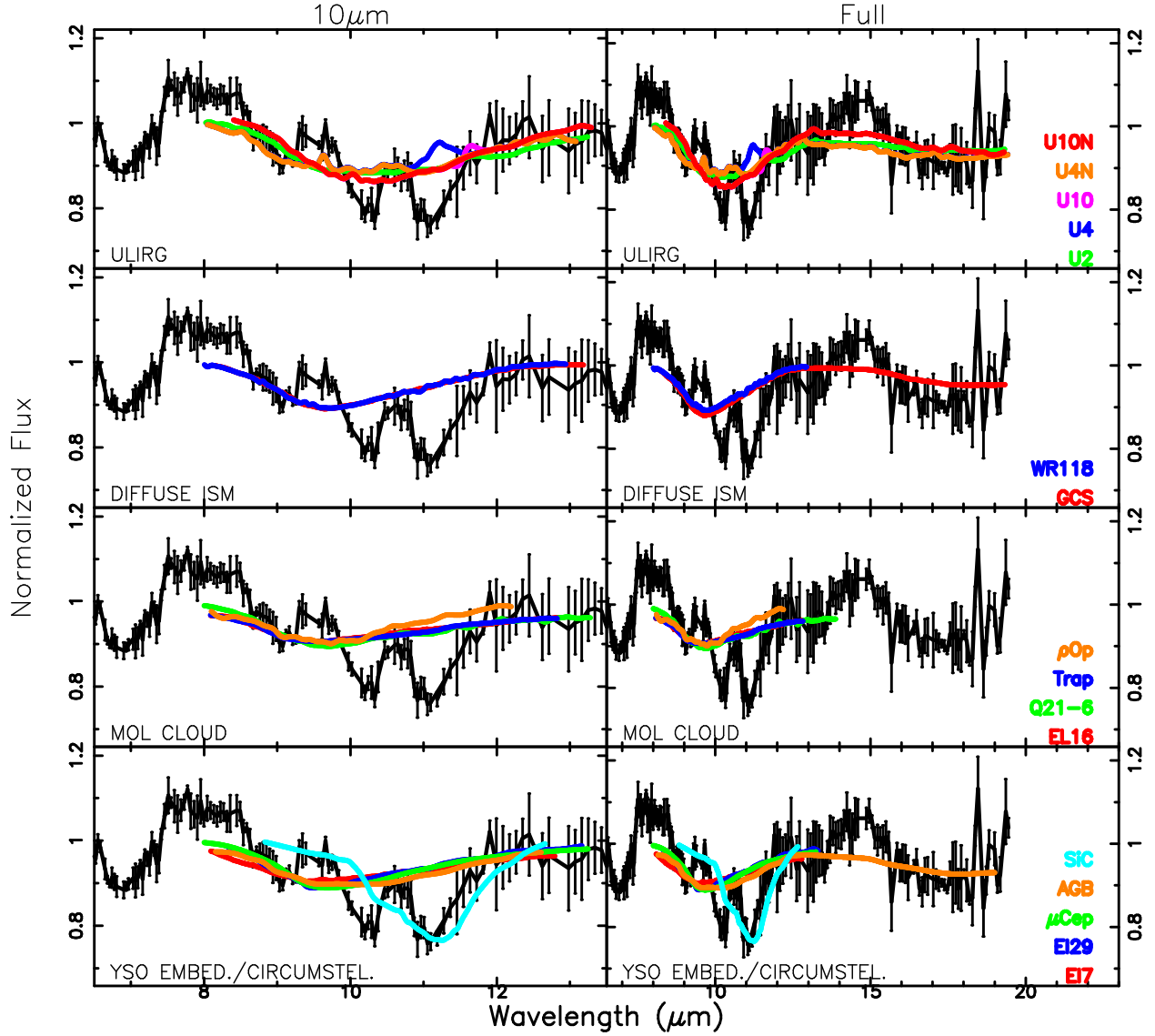


Fig. 4.— Continuum-normalized spectrum of PKS 1830-211, in the rest frame of the $z=0.886$ absorber, overlaid with fits from observed optical depth template profiles, divided by category. The left panels show fits performed solely over the $10 \mu\text{m}$ feature ($8.0\text{--}13.3 \mu\text{m}$). The right panels show the fits to the expanded range ($8.0\text{--}19.45 \mu\text{m}$), when available, otherwise a more limited fit is depicted. Abbreviations for the source names are as in Table 2. The rough agreement between the $10 \mu\text{m}$ and combined $10\text{--}18 \mu\text{m}$ template fits suggest that the continuum normalization constraints applied at long wavelengths are reasonable. None of the astrophysically observed optical depth profiles replicate the observed structure in the PKS 1830-211 absorber $10 \mu\text{m}$ region.

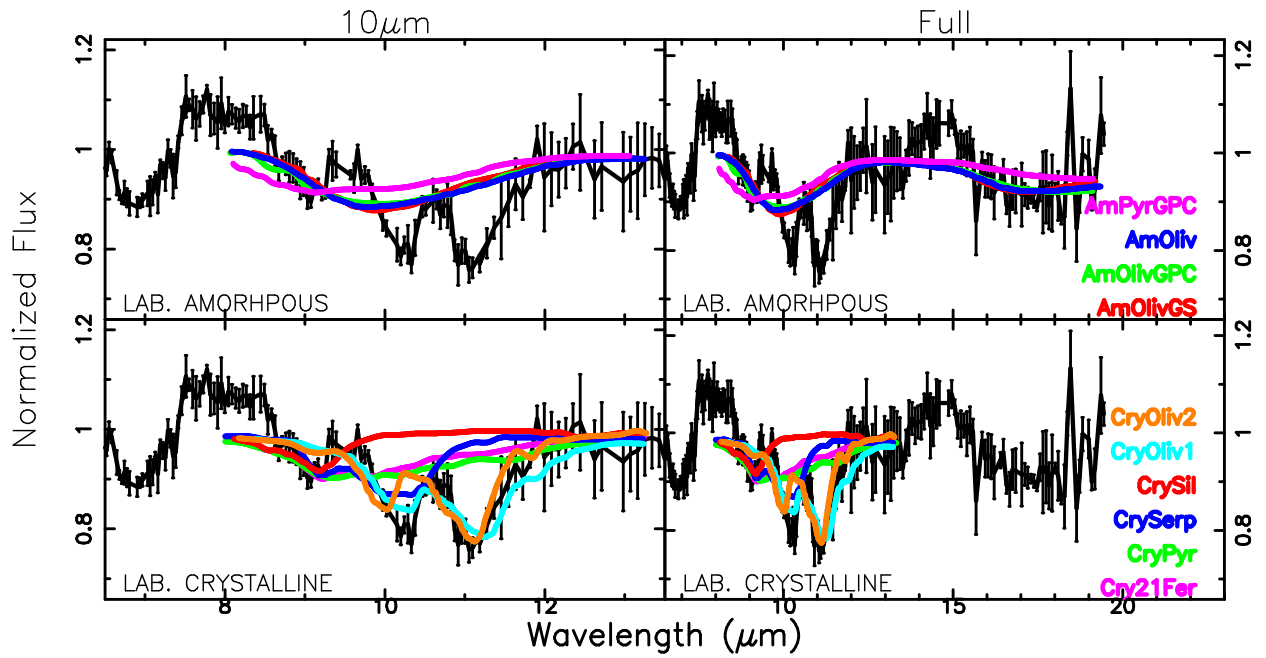


Fig. 5.— Similar to Figure 4, but for the laboratory amorphous and crystalline optical depth templates. Abbreviations for the source names are as in Table 3. The only profiles which reproduce the strong double-peaked profile within the 10 μm silicate feature region are the crystalline olivines.

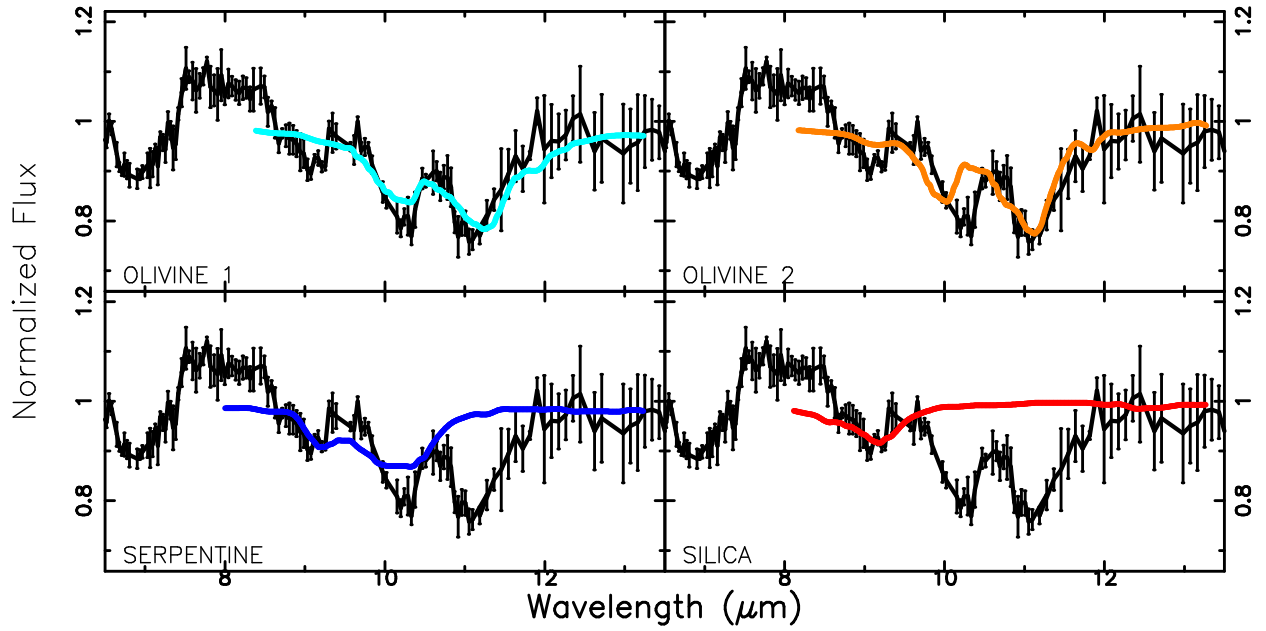


Fig. 6.— Four most viable profile fits to the $10\ \mu\text{m}$ absorption feature, overlaid on the PKS 1830-211 normalized flux curve, in the rest frame of the absorber. The top row illustrates the two crystalline olivine profile fits from Bowey & Adamson (2002). Note that while the central profile peak is well-matched by olivine 1, the rightmost peak is offset to slightly shorter wavelengths relative to olivine 1. The trend is reversed for olivine 2. This suggests the need for an olivine composition which is intermediate between the two profiles, or which exhibits slight variations in the grain morphology. Formally olivine 1 provides a slightly better fit, but neither of the olivine profiles reproduces the leftmost peak. This lower-wavelength peak could be fit by serpentine (which also contributes to the under-fit central peak) or by silica. We, thus, conclude that a mixture of olivine and one of these materials is the most likely component of the silicate dust.

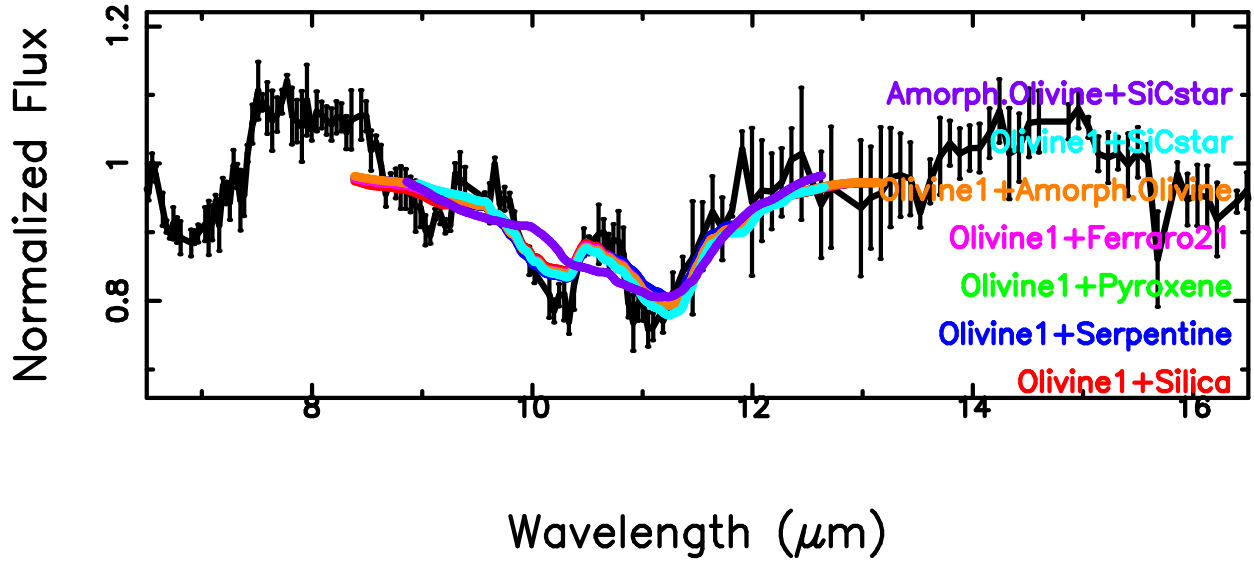


Fig. 7.— Bi-variate fits combining the best-fitting olivine 1 profile with other templates, overlaid on top of the normalized flux curve for PKS 1830-211 in the rest-frame of the $z=0.886$ absorber. The best fit is produced by olivine 1 + silica, although in *every* case olivine 1 is the dominant component. The minimal relative contributions from the secondary constituents produces the visual similarity between the 6 different fits. We also illustrate the amorphous olivine + SiC combination, for comparison.

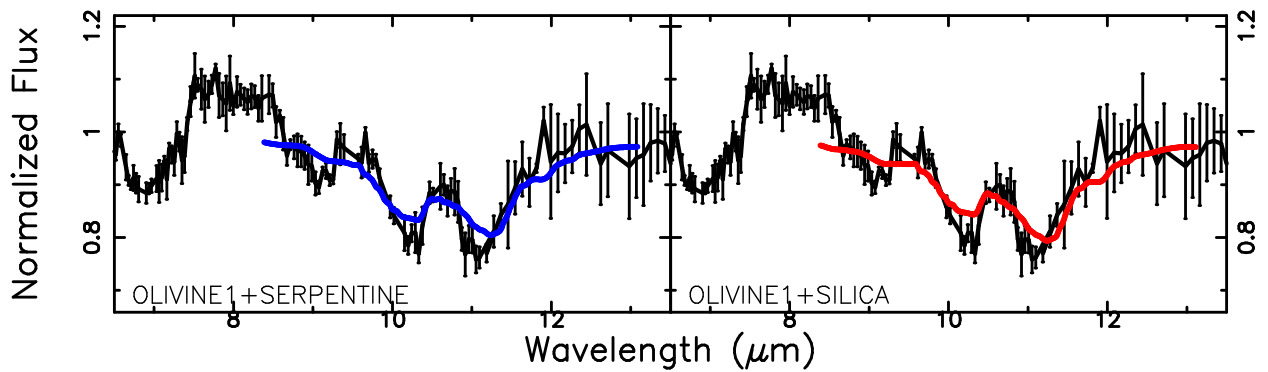


Fig. 8.— Bi-variate fits combining the olivine 1 and serpentine (left) and silica (right) optical depth profiles, overlaid on the PKS 1830-211 normalized flux curve in the rest-frame of the $z=0.886$ absorber. These two combinations formally produce the best fits, as suggested by Figure 6; although the improvement over the pure olivine 1 profile is slight.

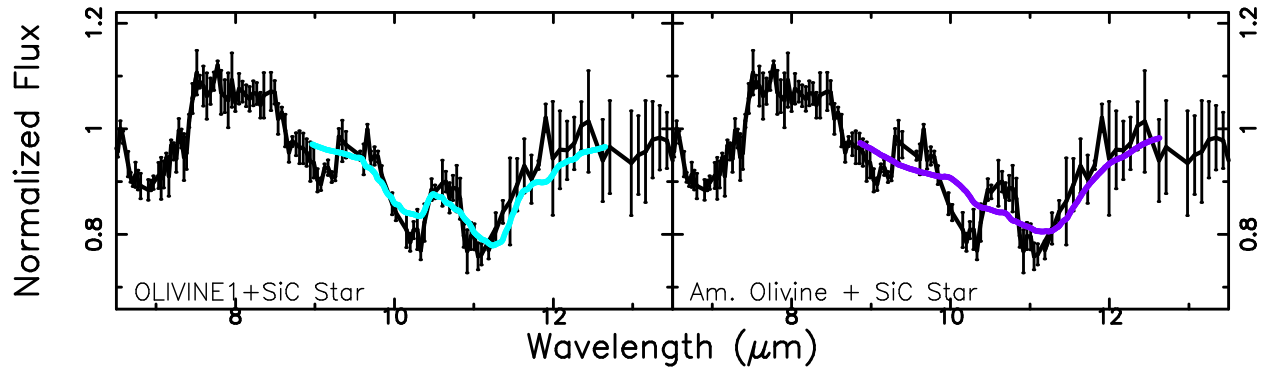


Fig. 9.— Bi-variate fits combining the olivine 1 and SiC profile (left) and amorphous olivine and SiC (right) optical depth profiles, overlaid on the PKS 1830-211 normalized flux curve in the rest-frame of the $z=0.886$ absorber. The combination of SiC with olivine 1 provides no significant improvement over the pure olivine 1 fit, while the combination of the SiC with amorphous olivine is an improvement over the pure amorphous olivine profile, although it is still not as good as the pure olivine 1 profile at fitting the data.

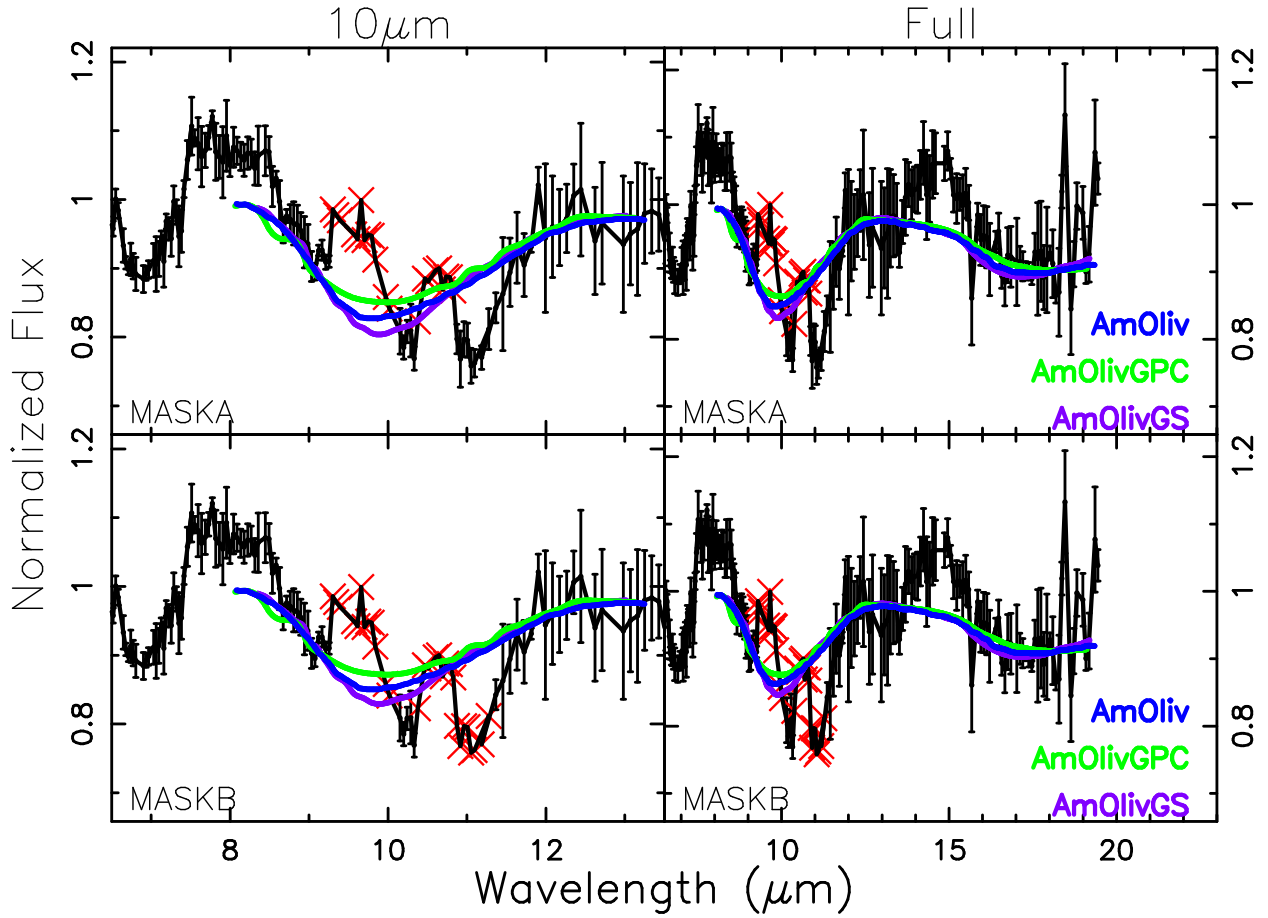


Fig. 10.— Illustration of the masked and normalized PKS 1830-211 spectrum in the rest-frame of the $z=0.886$ absorber, with the three amorphous olivine profile fits overlaid. The masked points are shown with red Xs, and no error bars. The left column shows the fit over only the $10 \mu\text{m}$ feature, while the right column shows the fit over the expanded range including $18 \mu\text{m}$. The top row shows mask A and the bottom row shows mask B, with the masks described in §4. The best fits occur for mask B, although these are weakly constrained in the $10 \mu\text{m}$ region

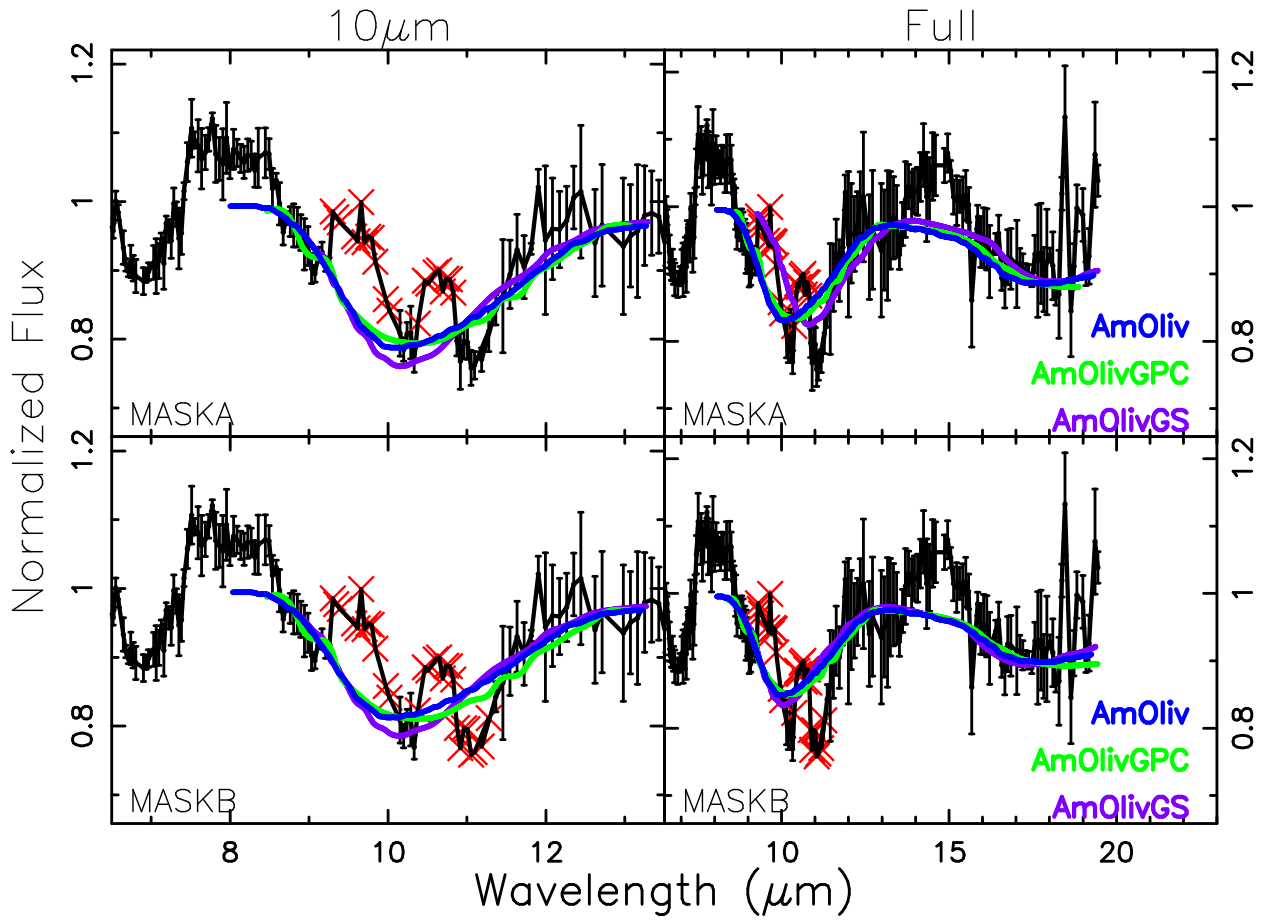


Fig. 11.— Similar to Figure 10, but illustrating the fits when both masking of PKS 1830-211 and wavelength-shifting of the profile are implemented.

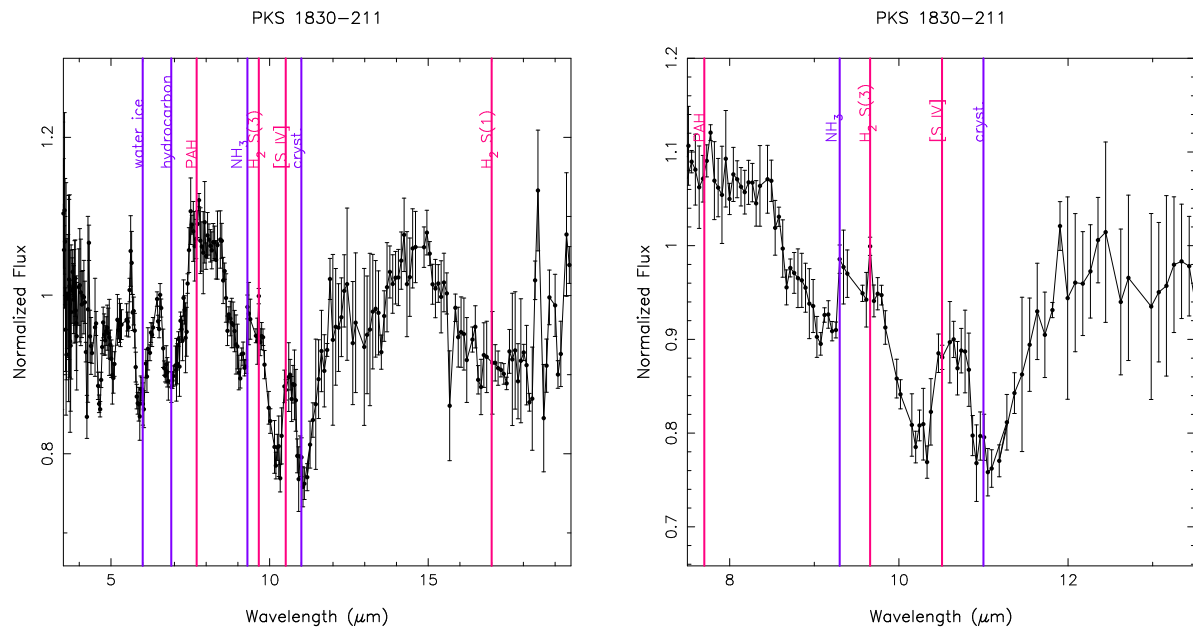


Fig. 12.— Normalized flux profile for PKS 1830-211 in the absorber rest-frame ($z=0.886$), overlaid with emission (pink) and absorption (purple) molecular and atomic transitions detected in other astrophysical objects. These features could be invoked, in combination with a broad amorphous silicate absorption feature, to explain the structure in the PKS 1830-211 spectrum.

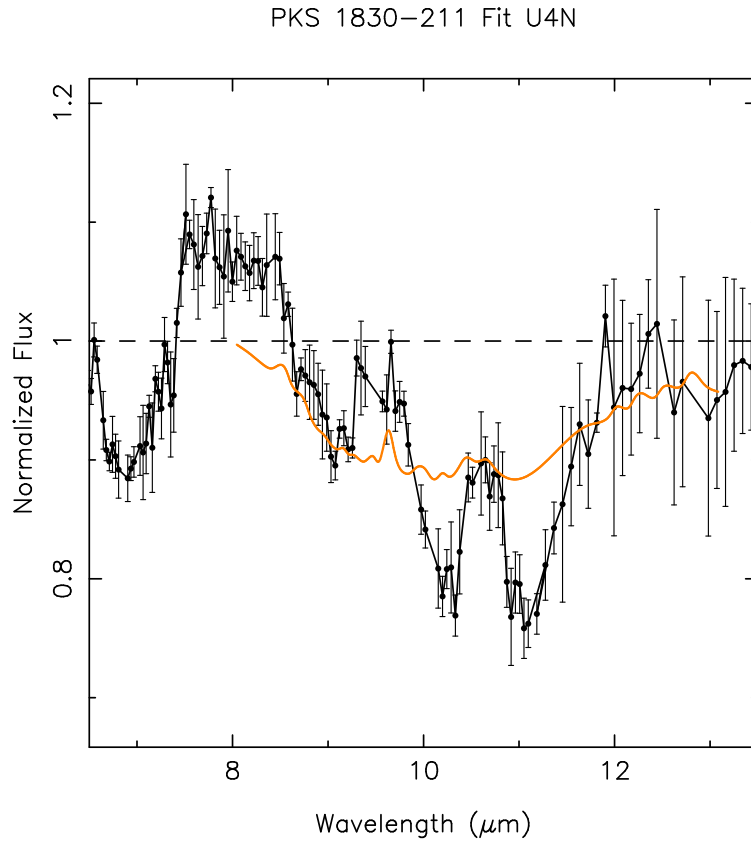


Fig. 13.— Normalized flux profile for PKS 1830-211, in the absorber-rest-frame, overlaid with the fit for the U4N modified ULIRG profile template. While the ULIRG emission/absorption features occur at approximately the correct wavelengths to explain the structure in the PKS 1830-211 spectrum, they are too narrow and/or shallow relative to the required underlying broad amorphous silicate feature.

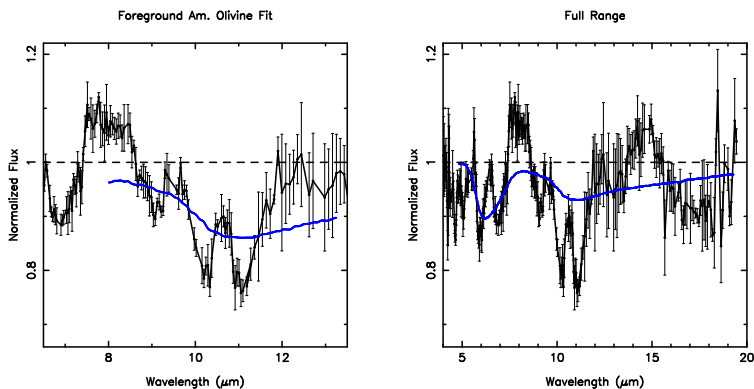


Fig. 14.— Normalized flux profile for PKS 1830-211, in the $z=0.886$ absorber-rest-frame, overlaid with an amorphous olivine fit to the presumed $z=0.19$ foreground galaxy silicate absorption. In the left panel we show the fitting results in the $8\text{--}13.3\ \mu\text{m}$ region, and in the right panel we show the results from fitting in the $4.8\text{--}19.4\ \mu\text{m}$ region. While the purported $10\ \mu\text{m}$ feature could instead be attributed to the $18\ \mu\text{m}$ feature of the $z=0.19$ foreground galaxy, as illustrated in the left panel, the corresponding $10\ \mu\text{m}$ silicate feature for the foreground galaxy is absent, as illustrated in the right panel. Instead, there is an emission feature present at rest wavelength of the $z=0.19$ galaxy $10\ \mu\text{m}$ silicate feature. Therefore, we do not believe that the structure we see in the PKS 1830-211 spectrum originates from a superposition of $10\ \mu\text{m}$ absorption from the $z=0.886$ quasar absorber and $18\ \mu\text{m}$ absorption from the $z=0.19$ foreground galaxy.